

# Analysis of Selected Models for Inelastic Electron Scattering in the KATRIN Gaseous Tritium Source

Master's thesis of

Fabian Leven

at the Institute of Experimental Particle Physics (ETP)  
of the Department of Physics  
at the Karlsruhe Institute of Technology

Reviewer: Prof. G. Drexlin  
Institute of Experimental Particle Physics, KIT  
Second Reviewer: Dr. K. Valerius  
Institute of Experimental Particle Physics, KIT  
Advisor: M. Sc. M. Machatschek  
Institute of Experimental Particle Physics, KIT

July 15th, 2018 – July 14th, 2019



# **Erklärung der Selbstständigkeit**

Ich versichere, dass ich diese Arbeit selbstständig verfasst habe und keine anderen als die angegebenen Quellen und Hilfsmittel benutzt habe, die wörtlich oder inhaltlich übernommenen Stellen als solche kenntlich gemacht und die Satzung des KIT zur Sicherung guter wissenschaftlicher Praxis in der gültigen Fassung vom 24.05.2018 beachtet habe.

Karlsruhe, den 14.07.2019, \_\_\_\_\_  
Fabian Leven

Als Prüfungsexemplar genehmigt von

Karlsruhe, den 14.07.2019, \_\_\_\_\_  
Prof. G. Drexlin



# Introduction

To our current knowledge, neutrinos are at the same time the most elusive and most abundant massive particles in the Universe. Their detection is challenging and pushes experiments at the edge of technical frontiers. Yet, their understanding might shed light on long standing open questions of modern physics: What is dark matter? Do Majorana particles exist? Why does matter predominate antimatter? What happened in the earliest stages of our Universe just after the Big Bang? And in all these regards, the yet unknown mass of neutrinos is a key physics parameter.

The KArlsruhe TRItium Neutrino (KATRIN) experiment aims to measure the effective mass of the electron antineutrino with an unprecedented sensitivity of 200 meV (90 % C.L.) based on tritium- $\beta$  decay. In order to provide this outstanding sensitivity KATRIN features i. a. a gaseous tritium source. Its special characteristics must be well controlled and understood. This thesis focuses on selected effects stemming from electrons scattering in said gaseous source. The effects were included in a high level analysis, meaning their impact on KATRIN's neutrino mass sensitivity was studied where possible.

## Outline

Chapter 1 is a brief introduction to neutrino physics with special emphasis on the neutrino mass.

Chapter 2 focuses on the setup of the KATRIN experiment and introduces a mathematical model of a KATRIN neutrino mass measurement.

Chapter 3 integrates the mathematical model into a statistical framework for a high level analysis, especially for neutrino mass inference.

Chapter 4 investigates a refinement of the mathematical model with regard to electrons scattering from gas molecules within KATRIN's gaseous source. Namely, the dependence of the inelastic scattering cross section on the energy of the incident electrons is studied.

Chapter 5 focuses on a preliminary model for the energy loss of electrons scattering inelastically from deuterium molecules. The model was established by a dedicated subgroup of the KATRIN collaboration based on KARIN data from October 2018. Its relation to KATRIN's sensitivity on the neutrino mass is investigated.

Chapter 6 summarizes the results, draws conclusions and offers an outlook.



# Contents

<b>Introduction</b>	<b>v</b>
<b>List of Figures</b>	<b>ix</b>
<b>List of Tables</b>	<b>xi</b>
<b>1. Neutrino Physics</b>	<b>1</b>
1.1. Neutrinos until the 1960s . . . . .	1
1.2. Neutrinos in the Standard Model of Particle Physics . . . . .	2
1.2.1. The Standard Model of Particle Physics . . . . .	2
1.2.2. Neutrino Properties . . . . .	3
1.3. Neutrino Mass Generating Mechanisms . . . . .	3
1.3.1. Neutrino Mass Terms . . . . .	4
1.3.2. Neutrino Mixing . . . . .	5
1.4. Neutrino Oscillations . . . . .	5
1.4.1. Demonstrative Formalism . . . . .	6
1.4.2. Experimental Considerations . . . . .	7
1.4.3. Experimental Case Study: The Solar Neutrino Problem . . . . .	7
1.4.4. Summary of Experimental Results . . . . .	8
1.5. Absolute Neutrino Mass Measurements . . . . .	8
1.5.1. Neutrino Masses from Cosmology . . . . .	8
1.5.2. Neutrino Masses from Neutrinoless Double- $\beta$ Decay . . . . .	10
1.5.3. Neutrino Masses from Kinematic Measurements . . . . .	10
<b>2. The KATRIN Experiment</b>	<b>13</b>
2.1. Experimental Setup . . . . .	13
2.1.1. Windowless Gaseous Tritium Source . . . . .	14
2.1.2. Rear Section . . . . .	15
2.1.3. Differential Pumping Section . . . . .	16
2.1.4. Cryogenic Pumping Section . . . . .	17
2.1.5. Pre and Main Spectrometer . . . . .	18
2.1.6. Detector Section . . . . .	21
2.2. THIS SECTION IS NOT YET STRUCTURED! The Integrated $\beta$ -Decay Spectrum Measured by KATRIN . . . . .	22
2.2.1. $\beta$ Decay Spectrum . . . . .	22
2.2.2. Detector Counts . . . . .	24
2.2.3. Discretization of the WGTS Volume . . . . .	25
2.2.4. Magnetic Bottle Effect . . . . .	25
2.2.5. Scattering Probabilities . . . . .	25
2.2.6. MAC-E Principle and Transmission Function . . . . .	26
2.2.7. Response Function . . . . .	28
2.2.8. Energy Loss Function . . . . .	28

2.2.9. Distribution of Pitch Angles . . . . .	29
2.2.10. Reconciliation . . . . .	31
2.2.11. Amendments . . . . .	31
2.3. A KATRIN Neutrino Mass Measurement . . . . .	31
<b>3. Statistical Methods and Neutrino Mass Inference at KATRIN</b>	<b>33</b>
3.1. The Maximum Likelihood Estimator . . . . .	33
3.2. The KATRIN Likelihood . . . . .	33
3.3. Confidence and Credible Intervals . . . . .	34
3.3.1. Bayesian Credible Intervals . . . . .	34
3.3.2. Frequentist Confidence Intervals . . . . .	34
3.4. Nuisance Parameters and the Profile Likelihood Method . . . . .	34
3.5. The KaFit and SSC Software Frameworks . . . . .	34
3.6. KATRIN’s Sensitivity to the Electron Antineutrino Mass . . . . .	34
<b>4. The Energy-Dependence of Inelastic Electron Scattering within the KATRIN Source Section</b>	<b>35</b>
4.1. Cross Section of Tritium- $\beta$ Electrons Scattering from Hydrogen Isotopologues	35
4.2. Motivation and Significance for the KATRIN Experiment . . . . .	36
4.3. An Energy-Dependent Scattering Model within the KATRIN Formalism .	37
4.3.1. Model Description . . . . .	37
4.3.2. Model Discussion . . . . .	39
4.4. Implementation of the Energy-Dependent Scattering Model . . . . .	39
4.4.1. Description of the Implementation . . . . .	39
4.4.2. Performance and Accuracy Considerations . . . . .	39
4.5. Effect on the Inferred Neutrino Mass . . . . .	40
4.5.1. Neutrino Mass Shift within a Standard KATRIN Measurement Interval	40
4.5.2. Neutrino Mass Shift in an Extended Measurement Interval . . . . .	40
4.6. Conclusion and Outlook . . . . .	40
<b>5. Parameter Inference Using an Energy Loss Model for Inelastically-Scattering Electrons Derived from KATRIN Data</b>	<b>45</b>
5.1. The Preliminary KATRIN Energy Loss Model . . . . .	45
5.2. Statistical Prerequisites . . . . .	45
5.2.1. Combination of Commissioning and Neutrino Mass Measurements .	45
5.2.2. Extension of the KaFit Software Framework . . . . .	46
5.3. A Sensitivity Study using the Recent Preliminary KATRIN Energy Loss Model . . . . .	47
5.4. Conclusion and Outlook . . . . .	47
<b>6. Conclusions and Outlook</b>	<b>49</b>
<b>Appendix</b>	<b>51</b>
A. Energy-Dependence of the Scattering Probabilities . . . . .	51
A.1. Modeling . . . . .	51
A.2. Numerical Evaluation . . . . .	52
B. Neutrino Mass Prior . . . . .	52
C. Likelihood Extensions . . . . .	53

# List of Figures

1.1.	Particles of the Standard Model of particle physics . . . . .	4
1.2.	Mixing parameters and mass ordering . . . . .	9
1.3.	Feynman graph of neutrinoless double-beta decay . . . . .	11
2.1.	KATRIN beamline . . . . .	14
2.2.	KATRIN windowless gaseous tritium source (WGTS) . . . . .	15
2.3.	KATRIN rear section . . . . .	16
2.4.	KATRIN differential pumping section (DPS) . . . . .	17
2.5.	KATRIN cryogenic pumping section (CPS) . . . . .	18
2.6.	Scheme of the KATRIN main spectrometer and the MAC-E filter principle. . . . .	19
2.7.	KATRIN detector section . . . . .	22
2.8.	Tritium $\beta$ spectrum . . . . .	23
2.9.	Scheme of the KATRIN main spectrometer and the MAC-E filter principle. . . . .	27
2.10.	KATRIN response function . . . . .	30
4.1.	Inelastic cross section for non-relativistic electrons scattering from molecular hydrogen isotopologues . . . . .	36
4.2.	Scattering probabilities . . . . .	42
4.3.	Run-time comparison between using an energy-dependent and -independent cross section . . . . .	43
4.4.	Neutrino mass shift due to an energy dependent inelastic scattering cross section . . . . .	44
A.1.	Numerical accuracy of the extended model for the scattering probabilities .	54



# List of Tables

1.1.	Neutrino sources for neutrino oscillation experiments . . . . .	7
1.2.	Overview of neutrino oscillation parameters . . . . .	10
1.3.	Limits on the the neutrino mass by double- $\beta$ decay experiments . . . . .	10
1.4.	Upper limits on absolute neutrino masses from kinematic measurements . .	11
4.1.	Energy-dependence of the inelastic scattering cross section . . . . .	37
4.2.	Scattering probabilities . . . . .	37



# 1. Neutrino Physics

This chapter is an introduction to neutrino physics. The primary aim is to give an experimentally-rooted definition of a neutrino. Therefore, in section 1.1 selected experimental milestones are outlined that led to today's description of a neutrino in the so-called Standard Model of particle physics (SM). In 1.2 follows an outline of the SM and how it relates to the neutrino. Thereafter, special attention is paid to the neutrino mass: First, in section 1.3, the formalism that incorporates masses in the SM is summarized in. Second, in section 1.4, the so-called neutrino oscillations are introduced. Corresponding experiments proved that neutrinos have mass. Third, in section 1.5, experiments for an absolute neutrino mass measurement are presented because as such they relate particularly to the KATRIN experiment.

## 1.1. Neutrinos until the 1960s

Albeit the neutrino as a possible particle was not postulated until 1930, its rich scientific history might be seen as already heralded during the preceding 35 years.

In 1895, Becquerel reported results on experiments with phosphorescent substances, especially uranium salts, on photographic plates [Bec95]. These experiments are marked as the discovery of radioactivity and triggered manifold subsequent investigations.

In 1899, Rutherford published a classification of radioactive decays into  $\alpha$  and  $\beta$  types according to their penetration strength [Rut99].

In 1900, Becquerel determined the mass-charge ratio of  $\beta$ -decay particles and identified them as the electron previously described by Thomson [Bec00] [Tho97].

In 1914, Chadwick measured a continuous electron energy spectrum in the  $\beta$  decay ( $\beta$  spectrum) of lead-214 and bismuth-214 [Cha14].

In 1927, Ellis and Wooster conducted a calorimetric measurement of the  $\beta$ -decay energy of radium and demonstrated that the continuity of the  $\beta$  spectrum was intrinsic to the decay as opposed to be caused by secondary effects as e.g. scattering of the electrons within an atom [EW27].

In 1930, a  $\beta$  decay was thought of as a two-body decay  ${}^zA \rightarrow {}^{z+1}B + e^-$ . Assuming conservation of energy and momentum, in a two-body-decay the momenta of the daughter particles B and  $e^-$  are solely determined by their masses and the “energy content”, as Bohr put it, of the parent particle A. According to Bohr, there was no reason to believe that different nuclei of the same element A should have a different energy content in a  $\beta$  decay. Hence, the continuity of the  $\beta$  spectrum could not be explained [Boh32]. As a possible solution Pauli suggested the  $\beta$  decay to be a three-body decay and postulated an electrically neutral particle that carries part of the decay energy [PW+08].

In 1934, Fermi developed a quantitative theory of  $\beta$  decay that could describe the preceding experimental results. It comprises a four-fermion contact interaction respectively a

three-body-decay model. It was the first description of the so-called “weak interaction”. Furthermore, Fermi coined the term “neutrino” for the particle postulated by Pauli [Fer34]. Fermi’s theory inspired the idea to use the so-called “inverse  $\beta$  decay” or “neutrino capture” to detect neutrinos, which in today’s nomenclature is written as

$$\bar{\nu}_e + p^+ \rightarrow n + e^+.$$

In 1956, Cowan and Reines published results of a corresponding experiment. It was conducted using the sufficiently high neutrino flux of the nuclear reactor of the Savannah River Plant. The neutrinos originating in the reactor passed a tank of water and cadmium chloride triggering the above process. The emerging neutron was captured by the cadmium which emitted a photon in a 3 MeV to 11 MeV range. The emerging positron annihilated with an electron which produced two photons of 0.5 MeV each. A coincidence measurement of the corresponding photons enabled discriminating signal and background events. Based on their results they reported the discovery of the free neutrino [CR+56].

In the same year, 1956, Lee and Yang published an article on parity conservation. Parity conservation implies that a mirrored physical process behaves the same as its non-mirrored counterpart. They pointed out that parity conservation might be violated in weak interactions and suggested several probing methods [LY56].

In 1957 Wu et al. conducted one of the corresponding probing methods based on  $\beta$  decay. The parity operation respectively “the mirroring” corresponded a change of the magnetic field orientation in the experiment. The results showed that parity is violated [WA+57].

In 1958, Goldhaber et al. measured the helicity  $H$  of the neutrino. Its helicity is defined as  $H = \hat{\sigma} \cdot \hat{p}$ , where  $\hat{\sigma}$  is the spin unit vector and  $\hat{p}$  is the momentum unit vector of the neutrino. The experiment found  $H = -1$  which corresponds to a maximal parity violation. In other words, only left-handed neutrinos and right-handed antineutrinos interact weakly [GG+58].

In 1962, Danby et al. reported on a second type of neutrinos. A beam of pions generated at the Alternating Gradient Synchrotron in Brookhaven decayed according to  $\pi^\pm \rightarrow \mu^\pm + \bar{\nu}$ . The emerging neutrinos penetrated a 13.5-meter iron shield wall and their interaction were detected in a 10-t aluminum spark chamber. The observed interactions were path-like as opposed to shower-like, which implied the production of muons as opposed to electrons. This was marked as the discovery of the muon neutrino [DG+62].

The attempts to uniformly describe the manifold discoveries in the field of particle physics in a combined theory converged over the course of the second half of the 20th century into the so-called SM.

## 1.2. Neutrinos in the Standard Model of Particle Physics

This section introduces concepts of the Standard Model of particle physics (SM) in a condensed manner. It aims at giving a description of relevant particle properties in section 1.2.1 and relating them to neutrinos in section 1.2.2.

### 1.2.1. The Standard Model of Particle Physics

The SM is a gauge quantum field theory exhibiting the gauge symmetry  $SU(3) \times SU(2) \times U(1)$ . As such it can be formulated using the principle of least action and a Lagrangian density  $\mathcal{L}$  depending on fields and their derivatives [Zee03]. Albeit it can not account for all known physical phenomena, within its known boundaries, the SM is a well-tested and established theory, which is evident by e.g. the extensive Review of Particle Physics of the Particle Data Group [Tan+18].

## General Particle Properties

### ToDo

[Find text book about SM to put more citations.] The gap between fields and particles can be bridged as follows: If “[i]n region 1 in spacetime there exists a source that sends out a ‘disturbance in the field’, which is later absorbed by a sink in region 2 in spacetime[,] experimentalists choose to call this a particle” [Zee03]. Intrinsic particle properties can be derived from the relation of their associated fields to the Lagrangian density. E.g., a particle’s mass is encoded by the Yukawa coupling of its field to the higgs doublet within the higgs mechanism [Hig64]. A further intrinsic property is a particle’s spin, that takes either half-integer values in units of  $\hbar$  for fermions or integer values for bosons. A particle’s flavor is its eigenstate with respect to the weak interaction, which is described by the  $SU(2) \times U(1)$  subgroup (Glashow-Weinberg-Salam model [Gla61; Wei67; Sal68]). According to Noether’s theorem, each symmetry conserves an associated charge [Noe18]. In the case of the  $SU(2) \times U(1)$  symmetry, the associated charges are called isospin  $\mathbf{T} = (T_1, T_2, T_3)^T$  and hypercharge  $Y$ . A derivative from these charges is the electric charge  $Q = T_3 + \frac{1}{2}Y$ . In that sense, each particle has an associated antiparticle, that carries the opposite electric charge. As mentioned in the historical overview (section 1.1), a theory consistent with experiment must violate parity. Such theories are called chiral [Zee03]. The SM is a chiral theory and thus its fields can be decomposed in left- and right handed components.

Figure 1.1 depicts the particles of the SM along with their selected properties mass and electric charge. It also shows a further categorization within the fermions into quarks and leptons.

### 1.2.2. Neutrino Properties

With reference to the particle properties listed in the previous section 1.2.1, a neutrino can be described as follows: A neutrino carries a spin of  $1/2\hbar$ . Thus, it is a fermion; It is categorized as a lepton; It has an electric charge of 0; And there are only left-handed neutrinos and right-handed antineutrinos.

The mass of a neutrino will be discussed separately within the following chapters.

A neutrino exists in three flavors, typically denoted as  $\nu_e$ ,  $\nu_\mu$  and  $\nu_\tau$ . Some additional remarks about the neutrino flavors can be made: First, the historical overview (section 1.1) mentions the discovery of the electron and muon flavor, but it was not until 2001 that the tau neutrino was discovered by the DONUT collaboration [Kod+01]. Second, a precision measurement of the width of the  $Z^0$ -boson resonance  $\Gamma_Z = (2.68 \pm 0.15) \text{ GeV}$  at the Large Electron Positron Collider (LEP) in the 1990s yielded a number of light neutrino flavors consistent with three. In this context, “light” refers to a neutrino mass smaller than half the mass  $M_Z = (91.174 \pm 0.070) \text{ GeV}$  of the  $Z^0$  boson [Acc+98]. (It should be noted, that this refers to weakly interacting neutrino flavors. Sterile neutrinos with a lower mass as an extension of the SM are not ruled out[OW08].)

## 1.3. Neutrino Mass Generating Mechanisms

Section 1.4 lists experiments that proof that neutrinos have mass. However, in the standard model as described in section 1.2 the neutrino masses are assumed to be 0, but an extension is possible. The corresponding so-called mass terms are introduced in section 1.3.1. The neutrino-mass formalism also introduces the so-called neutrino mixing that is described in section 1.3.2.

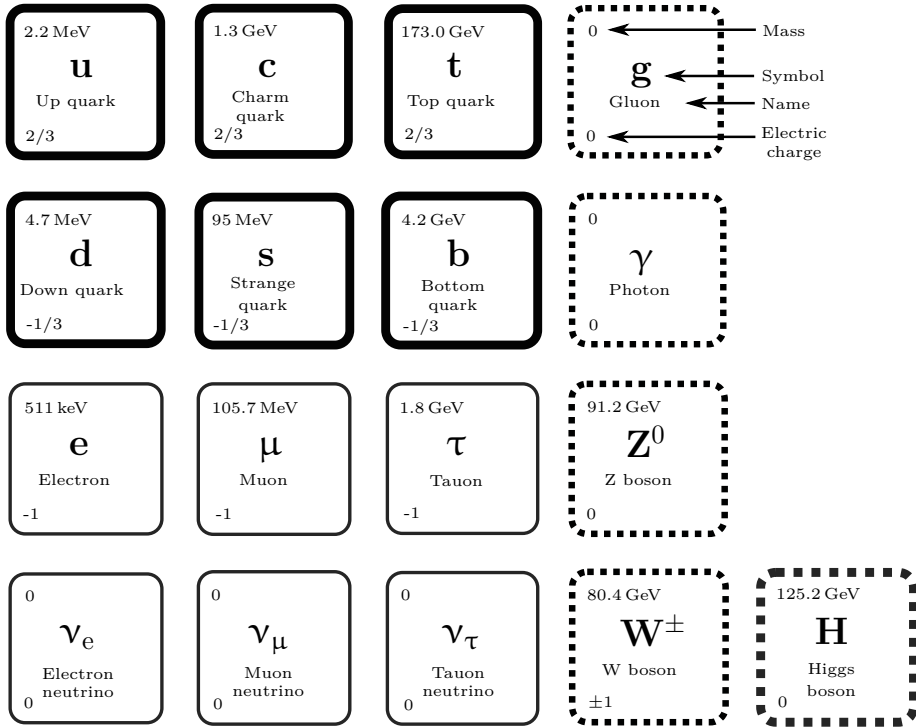


**Figure 1.1.: Standard Model of particle physics.** The diagram illustrates possible categorizations of particles within the SM. The fermions are framed continuously and the bosons dotted. Among the fermions the so-called quark sector is marked by a thick frame and the so-called lepton sector by a thin one. The first three columns show the fermions; and the fourth and the fifth the bosons. While the bosons in the fourth column carry a spin of 1, the higgs boson in the fifth column marked with a thicker frame carries a spin of 0. Also shown are the particle masses in natural units and their electric charge in units of the absolute electron charge. All quantities along with uncertainties can be found in the Review of Particle Physics [Tan+18]. (Illustration adapted from [Sei19])

### 1.3.1. Neutrino Mass Terms

For a theory to account for neutrino masses, its Lagrangian density must exhibit corresponding mass terms. According to [Zub11] the formalism can be summarized: The form of a mass term is given by the Dirac equation, which is produced by applying the principle of least action to a suitable Lagrangian density  $\mathcal{L}$ . The mass terms have to be quadratic in the fermion fields  $\psi$  and must leave the Lagrangian density hermitian. Furthermore, a field  $\psi$  must have a left- and right-handed component in order for the mass terms not to vanish. Two possible term forms are named after Dirac and Majorana. Whether one or a mixture of both forms correspond the neutrino's reality is an open question.

#### Dirac Masses

A Dirac mass term with mass  $m_D$  split in its chiral components (Weyl spinors)  $\psi_{L,R}$  has the form [Zub11]

$$\mathcal{L}_D = -m_D \bar{\psi} \psi = -m_D (\bar{\psi}_L \psi_R + \bar{\psi}_R \psi_L). \quad (1.1)$$

Applying this to neutrinos it requires both a left- and a right-handed Dirac neutrino. Right-handed neutrinos have not yet been observed. If they exist, they do not interact weakly and hence are called sterile.

## Majorana Masses

For Majorana mass terms the CP-conjugate  $\psi^C$  of a fermion spinor  $\psi$  is used. It should be noted that if  $\psi$  is left-handed,  $\psi^C$  is right-handed and vice versa. Then, a Majorana field  $\phi$  can be defined and a corresponding mass term  $\mathcal{L}_M$  with a mass  $m_M$  be constructed [Zub11]

$$\phi = \psi + \psi^C \quad \mathcal{L}_M = -\frac{1}{2}m_M \bar{\phi}\phi. \quad (1.2)$$

As  $\phi^C = \phi$ , the described Majorana particle is its own antiparticle, which due to charge conservation is only possible for neutral particles, such as a neutrino.

### 1.3.2. Neutrino Mixing

If neutrinos have mass, their mass eigenstates  $|\nu_i\rangle$  ( $i \in \{1, 2, 3\}$ ) of the free Hamiltonian need not be identical to their flavor eigenstates  $|\nu_\alpha\rangle$  ( $\alpha \in \{e, \mu, \tau\}$ ) of the weak interaction [Zub11]. In case they differ, there must be a basis-change matrix. Such a matrix was introduced by Maki, Nakagawa and Sakata in order to explain the so-called neutrino oscillations (see section 1.4) predicted by Pontecorvo [Pon58; MNS62]. Therefore, the matrix  $U$  for a basis change is called Pontecorvo-Maki-Nakagawa-Sakata matrix (PMNS matrix)

$$|\nu_\alpha\rangle = \sum_i U_{\alpha i} |\nu_i\rangle. \quad (1.3)$$

As a complex unitary matrix  $U$  can be expressed by six parameters. A possible choice are three angles  $\theta_{12}, \theta_{23}, \theta_{13} \in [0, 2\pi)$ , a phase  $\delta \in [0, 2\pi)$  and two Majorana phases  $\alpha, \beta \in [0, 2\pi)$ :

$$U = \begin{pmatrix} 1 & 0 & 0 \\ 0 & \cos \theta_{23} & \sin \theta_{23} \\ 0 & -\sin \theta_{23} & \cos \theta_{23} \end{pmatrix} \begin{pmatrix} \cos \theta_{13} & 0 & \sin \theta_{13} e^{-i\delta} \\ 0 & 1 & 0 \\ -\sin \theta_{13} e^{i\delta} & 0 & \cos \theta_{13} \end{pmatrix} \begin{pmatrix} \cos \theta_{12} & \sin \theta_{12} & 0 \\ -\sin \theta_{12} & \cos \theta_{12} & 0 \\ 0 & 0 & 1 \end{pmatrix} \begin{pmatrix} 1 & 0 & 0 \\ 0 & e^{i\alpha} & 0 \\ 0 & 0 & e^{i\beta} \end{pmatrix}. \quad (1.4)$$

These parameters are called neutrino mixing parameters. It should be noted that  $\delta$  is also called “CP-violating” phase. Here,  $P$  stands for parity conjugation as it was explained in section 1.1; and  $C$  for electric charge conjugation that follows the same idea with a sign change of the electric charge instead of the position vector. Why  $\delta \neq 0$  implies  $CP$ -violation is shown in section 1.4.1.

One of the consequences of neutrino mixing, namely neutrino oscillations, will be explained in the following section 1.4.

## 1.4. Neutrino Oscillations

The term “neutrino oscillations” refers to the neutrino’s change of flavor during propagation. In other words, neutrinos might be detected in another flavor than they originated in. Section 1.4.1 introduces a demonstrative formalism that aims at showing the link between oscillations and the masses of neutrinos. Neutrino oscillations also depend on the neutrino mixing parameters introduced in section 1.3.2. The accessibility of these mixing parameters and neutrino masses via neutrino oscillation experiments will be evaluated in section 1.4.4. Neutrino oscillation experiments are manifold. As an exemplary case study the so-called “solar neutrino problem” is discussed in section 1.4.3. Finally, the experimental results on neutrino oscillations will be summarized in section 1.4.4.

### 1.4.1. Demonstrative Formalism

According to [Zub11] a formula demonstrating neutrino oscillations can be derived: Using the PMNS matrix  $U$  from equation (1.4) the evolution of a neutrino's flavor eigenstate on a one-dimensional path starting at position  $x = 0$  at time  $t = 0$  with momentum  $p_i$  and energy  $E_i$  of its mass eigenstates  $|\nu_i\rangle$  is

$$|\nu_\alpha(x, t)\rangle = \sum_i U_{\alpha i} e^{-i(E_i t - p_i x)} |\nu_i\rangle. \quad (1.5)$$

This leads to the transition amplitudes

$$A(\alpha \rightarrow \beta)(t) = \langle \nu_\beta | \nu_\alpha(x) \rangle = \sum_i U_{\beta i}^* U_{\alpha i} e^{-i(E_i t - p_i x)t} \quad (1.6a)$$

$$A(\bar{\alpha} \rightarrow \bar{\beta})(t) = \langle \bar{\nu}_\beta | \bar{\nu}_\alpha(x) \rangle = \sum_i U_{\beta i} U_{\alpha i}^* e^{-i(E_i t - p_i x)t}. \quad (1.6b)$$

It should be noted that if  $\Rightarrow U \neq U^*$ , equation (1.6) implies  $CP$ -violation. In reference to section 1.3.1 it holds  $U \neq U^* \Leftrightarrow \delta \neq 0$  justifying that  $\delta$  is called  $CP$ -violating phase.

The following assumptions allow for a simple and demonstrative form of the transition probability:

- The neutrinos are relativistic:
  - Their momentum equals approximately their energy which is by far larger than their mass  $p_i \approx E_i \gg m_i$ . This also implies that the energy can be expanded in the mass-momentum-ratio  $m_i/p_i$ .
  - They travel the distance  $x = L = ct$  at the speed of light  $c$ .
- All neutrino generations have approximately the same momentum  $E \approx p \approx p_i$ .
- The  $CP$ -violating phase vanishes  $\delta = 0$ . (This assumption is not necessary, but simplifies the expression for the transition probability significantly. See [Zub11] for  $\delta \neq 0$ .)

Then, the transition probability from one flavor  $\alpha$  to another  $\beta$  in dependence of the neutrino masses and mixing parameters is

$$\begin{aligned} P(\alpha \rightarrow \beta)(L) &= |\langle \nu_\beta | \nu_\alpha(L) \rangle|^2 \\ &= \delta_{\alpha\beta} - 4 \sum_i \sum_{j>i} U_{\alpha i} U_{\alpha j} U_{\beta i} U_{\beta j} \sin^2 \left( \frac{(m_i^2 - m_j^2)}{4} \frac{L}{E} \right). \end{aligned} \quad (1.7)$$

Equation (1.7) shows oscillatory behavior if the mass of at least two flavors differ and the corresponding off-diagonal elements of the PMNS matrix  $U$  are non-vanishing. Furthermore, neutrino oscillation experiments are sensitive to the difference of squared masses

$$\Delta m_{ij}^2 = |m_i^2 - m_j^2|, \quad (1.8)$$

which only yields two independent observables for three masses. Thus, these experiments cannot be used to determine the absolute mass scale of neutrinos.

### 1.4.2. Experimental Considerations

According to equation (1.7), the ratio  $L/E$  determines the sensitivity of an experiment to the oscillation parameters given by the PMNS matrix  $U$  (mixing parameters) and  $\Delta m_{ij}^2$  (mass ordering).  $L$  can be tuned by placing the detector in a suitable distance from a Earth-based neutrino source.  $E$  can either be tuned by using e. g. particle accelerators as source or if the source exhibits an energy spectrum like e.g. the Sun.

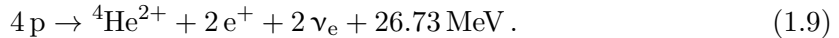
Furthermore, two detection channels can be distinguished. If, on one hand, an experiment is sensitive to the neutrino flavor emitted by the surveyed neutrino source, it can detect a weakening of the neutrino flux. This is referred to as disappearance channel. If, on the other side, an experiment is sensitive to a different neutrino flavor than the surveyed neutrino source emits, this is referred to as appearance channel.

There are four major neutrino sources that can be used to measure the mixing parameters and the mass ordering. They are listed in table 1.1. For each source multiple experiments exist [Zub11]. Not all experiments will be discussed here. Instead the following section 1.4.3 discusses the so-called “Solar Neutrino Problem” as an exemplary case study on solar neutrino experiments.

### 1.4.3. Experimental Case Study: The Solar Neutrino Problem

The term “Solar Neutrino Problem” refers to the mismatch of the total neutrino flux arriving on Earth predicted by the standard solar model (SSM) and measured by, first, the Homestake and, later, other experiments. In this section the problem is briefly described and its resolution developed.

In the end of the 1930s, Bethe, von Weizsäcker and Critchfield showed that there are two main fusion cycles in the Sun, the so-called cno and pp cycle. The latter is the primary source of solar neutrinos [Wei38; BC38; Bet39]. Its multi-step reaction can be summarized as [Zub11]



Its initial reaction and the one with the broadest neutrino energy spectrum (from below 0.1 to  $\sim 11$  MeV [Tan+18]) are



It should be noted, that only electron neutrinos are produced in the Sun. Starting from the 1970s the solar electron neutrino flux was measured; the first time by the Homestake

**Table 1.1.: Neutrino sources for neutrino oscillation experiments.** Listed are different neutrino sources and which neutrino flavors they emit [Zub11]. Furthermore, the oscillation parameters they are sensitive to are tabulated along with an example experiment.

source	flavors	sensitive to	example experiment
nuclear power plants	$\bar{\nu}_e$	$\sin \theta_{13}$	Double Chooz [AA+16]
accelerators	$\nu_e, \nu_\mu, \bar{\nu}_e, \bar{\nu}_\mu$	$\sin \theta_{12}, \sin \theta_{23}, \Delta m_{12}^2, \Delta m_{23}^2$	MiniBooNE [AA+09]
atmosphere	$\nu_e, \nu_\mu, \bar{\nu}_e, \bar{\nu}_\mu$	$\sin \theta_{23}, \Delta m_{23}^2$	Super-Kamiokande [Fuk+98]
the Sun	$\nu_e$	$\sin \theta_{12}, \Delta m_{21}^2$	SNO [AA+13]

experiment using the inverse beta decay of  $^{37}\text{Cl}$ . It could detect electron neutrinos with an energy threshold of 813 keV. The measured flux was one third of the prediction by the SSM [CD+98; BPB01]. This is marked as the beginning of the solar neutrino problem. The experiments GALLEX/GNO and SAGE confirmed the results, where the latter could detect electron neutrinos with an energy threshold of 233 keV [Kir98; AB+05; AG+09]. Starting from 1999 the SNO experiment measured the neutrino flux of all flavors. It used 1000 t of heavy water  $\text{D}_2\text{O}$  to detect electron neutrinos via charged currents as well as all flavors via neutral currents and neutrino-electron scattering. In order to fully explain the flux data, the so-called Mikheyev-Smirnov-Wolfenstein effect (MSW effect) had to be respected [Wol78; MS86]: Electron neutrinos can undergo charged current interactions with surrounding electrons in a coherent forward scattering process, which alters the flavor transition amplitude. This effect is only significant in areas of high electron densities, such as the Sun. Taking these matter-mediated oscillations into account, the measured flux of all flavors of the  $^8\text{B}$  neutrinos, equation (1.10), was in accordance with the electron neutrino flux predicted by the SSM [AA+13]. Thus, the solar neutrino problem was resolved.

#### 1.4.4. Summary of Experimental Results

This section summarizes the results obtained from neutrino oscillation experiments. The neutrino oscillation parameters consist of the squared neutrino mass differences, equation (1.8), and the mixing parameters of the PMNS matrix, equation (1.4). It should be noted first, that the MSW resonance of solar neutrinos requires  $m_1 < m_2$ , which allows for two possible mass orderings [Zub11]:

1. normal ordering  $m_1 < m_2 < m_3$  and
2. inverted ordering  $m_3 < m_1 < m_2$ .

For these two cases a combination of recent experimental results for the neutrino oscillation parameters is given in table 1.2 and illustrated in Figure 1.2. All in all, neutrino oscillations are experimentally verified and proof that neutrinos have mass.

### 1.5. Absolute Neutrino Mass Measurements

The absolute masses of neutrinos are unknown and, as shown in section 1.4.1, neutrino oscillations are only sensitive to squared mass differences. This section presents methods to probe the absolute neutrino mass. The corresponding measurements fall into one of three categories [OW08]:

- cosmology (section 1.5.1),
- neutrinoless double  $\beta$  decay (section 1.5.2) or
- kinematic measurements of e.g.  $\beta$  electrons or the like (section 1.5.3).

#### 1.5.1. Neutrino Masses from Cosmology

In the early Universe, neutral particles such as light neutrinos could escape from areas of high mass density to areas of low mass density. As they carry away mass, the larger the neutrino mass, the stronger is the suppression of density fluctuations on small scales. In a mathematical formulation the so called power spectrum of the density contrast is examined. Corresponding data are e.g. obtained by the Sloan Digital Sky Survey (SDSS). This experiment records the sky's electromagnetic spectrum via telescope [DT+04]. Furthermore, the temperature anisotropies in the cosmic microwave background (CMB) encode information on the Universe's structure. The latest and most precise data are recorded by the PLANCK satellite [Agh+18]. Under the assumption that all mass states

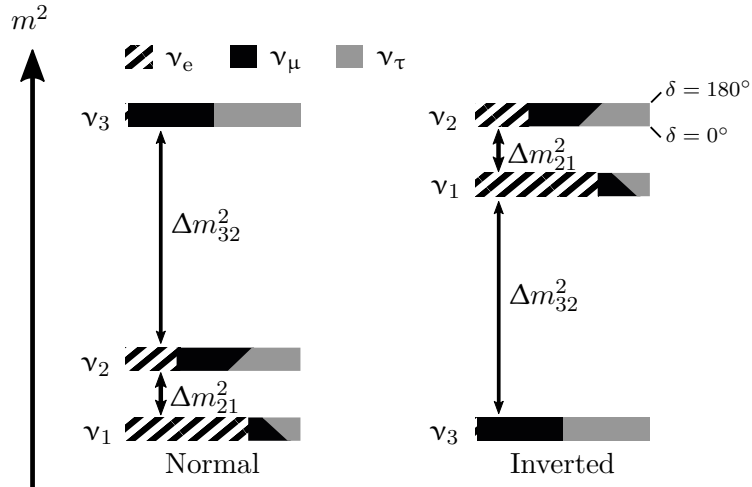


**Figure 1.2.: Mixing parameters and mass ordering.** The chart shows how the mass eigenstates  $\nu_i$  are composed of the flavor eigenstates  $\nu_\alpha$  in the normal and inverted mass ordering. The composition depends on the phase  $\delta$ . The mixing is shown for the two extreme cases  $\delta = 0^\circ$  (baseline) and  $\delta = 180^\circ$  (topline). (Adapted from [Sei19]. Numerical values can be found in [EG+19].)

contribute with the same number density cosmological observations are to first order only sensitive to the sum of all neutrino masses  $\sum_i m_i$ . A combination of the above data sets yields [YP+17]

$$\sum_i m_i < 0.14 \text{ eV} \quad (95\% \text{ C.L.}).$$

**Table 1.2.: Overview of neutrino oscillation parameters.** The table lists the observables and their best fit values along with the  $1\sigma$ -uncertainty range for normal and inverted ordering. (From [EG+19].)

observable	normal ordering	inverted ordering
$\sin \theta_{13}$	$0.310^{+0.013}_{-0.012}$	$0.310^{+0.013}_{-0.012}$
$\sin \theta_{23}$	$0.580^{+0.017}_{-0.021}$	$0.584^{+0.016}_{-0.020}$
$\sin \theta_{13}$	$0.02241^{+0.00065}_{-0.00065}$	$0.02264^{+0.00066}_{-0.00066}$
$\delta /^\circ$	$215^{+40}_{-29}$	$248^{+27}_{-29}$
$\frac{\Delta m_{21}^2}{10^{-5} \text{ eV}^2}$	$7.39^{+0.21}_{-0.20}$	$7.39^{+0.21}_{-0.20}$
$\frac{\Delta m_{31}^2}{10^{-3} \text{ eV}^2}$	$+2.525^{+0.033}_{-0.032}$	
$\frac{\Delta m_{32}^2}{10^{-3} \text{ eV}^2}$		$-2.512^{+0.034}_{-0.032}$

### 1.5.2. Neutrino Masses from Neutrinoless Double- $\beta$ Decay

Double- $\beta$  decay ( $2\nu\beta\beta$ ) is described as a nucleus of element  $X(Z, A)$  with  $Z$  protons and  $A - Z$  neutrons that decays to a daughter isotope  $Y(Z + 2, A)$  via two simultaneous  $\beta$  decays

$$X(Z, A) \rightarrow Y(Z + 2, A) + 2e^- + 2\bar{\nu}_e. \quad (1.11)$$

If the neutrino is its own antiparticle, respectively of Majorana type, the neutrino emitted in the first decay can be absorbed in the second decay resulting in a neutrinoless double decay ( $0\nu\beta\beta$ ). This would require the neutrino to have mass. Such a decay would manifest itself in a peak in the  $\beta$  spectrum two neutrino masses above the endpoint of the continuum [Zub11]. It should be noted, that this would violate lepton number conservation. The half-life of such a decay encodes the Majorana mass of the electron neutrino as a coherent sum of all neutrino masses using the PMNS matrix  $U$  from equation (1.4)

$$m_{\beta\beta} = \left| \sum_i U_{ei}^2 m_i \right|. \quad (1.12)$$

As  $U$  contains two unknown Majorana phases partial cancellation might occur. Hence, it is difficult to compare  $m_{\beta\beta}$  to masses obtained by other methods. The two most stringent upper limits on  $m_{\beta\beta}$  are listed in table 1.3.

### 1.5.3. Neutrino Masses from Kinematic Measurements

Several laboratory experiments, as well as the supernova event 1987A, have provided upper limits of absolute neutrino masses from the analysis of neutrino kinematics. Such experiments can not resolve the mass splitting between the squared mass eigenvalues.

**Table 1.3.: Limits on the the neutrino mass by double- $\beta$  decay experiments.** Listed are the two most stringent limits on  $m_{\beta\beta}$ , equation 1.12, given as ranges.

experiment	90 % C.L. upper limit on $m_{\beta\beta}$ (eV)
GERDA [Ago+18]	0.12–0.26
KamLAND-Zen [GG+16]	0.05–0.16

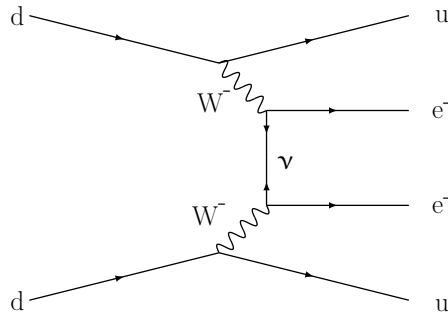


**Figure 1.3.: Feynman graph of neutrinoless double- $\beta$  decay.** The graph depicts the simultaneous decay of two neutrons into two protons where the down quarks decay to up quarks. The two emitted neutrinos annihilate in a Majorana transition.

**Table 1.4.: Upper limits on absolute neutrino masses from kinematic measurements.** The table lists upper limits on absolute neutrino masses for different neutrino flavors.

flavor	measurement basis	upper limit	reference
$\nu_e$	neutrinos from Supernova 1987A	5.7 eV (95 % credible interval)	[LL02]
$\nu_\mu$	muon decay	17 keV (90 % C.L.)	[AB+96]
$\nu_\tau$	tau decay	18.2 MeV (95 % C.L.)	[Bar+98]
$\bar{\nu}_e$	tritium- $\beta$ decay	2 eV (95 % C.L.)	[Tan+18]

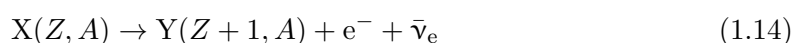
Therefore, the corresponding observable is a weighted sum of the  $N$  neutrino eigenmasses where the weights are the elements of the PMNS matrix from equation (1.4) [OW08]

$$m_{\nu_\alpha}^2 = \sum_i^N |U_{\alpha i}|^2 m_i^2. \quad (1.13)$$

With respect to the KATRIN experiment, the measurement of the mass of the electron antineutrino via  $\beta^-$ -decay kinematics is of special interest. Hence, this subject is examined more closely within this section. For completeness, aside from the upper limit on the mass of the electron antineutrino, table 1.4 also lists upper limits for other neutrino flavors obtained by kinematic measurements.

### Neutrino Masses from $\beta$ -decay Kinematics

In  $\beta^-$  decay



part of the released surplus energy generates the neutrino's mass. This leaves a signature in the  $\beta$  spectrum. In a neutrino mass experiment four criteria are important for a suitable  $\beta$  emitter [OW08]:

- The  $\beta$  emitter should have an energy spectrum with a relatively low endpoint, because in the uncertainty on the neutrino mass enter the input uncertainties of neutrino energy and momentum scaled up with the endpoint energy.
- The  $\beta$  emitter must have a sufficiently high activity to provide statistically relevant count rates.
- The  $\beta$  decay should be super-allowed in order for the nuclear matrix element of the decay process to be energy independent.
- The  $\beta$ -emitter molecule should be as simple as possible to allow for a theoretical treatment of its decay kinematics such as the final state of the decay-daughter molecule.

Tritium is an ideal candidate with respect to these criteria[OW08]. The corresponding measurement principle will be explained more closely in the following chapters about the KATRIN experiment. However, KATRIN has predecessor experiments. The most recent two experiments based on tritium- $\beta$  decay in Mainz and Troitsk obtained a combined upper limit on the electron antineutrino mass of [KB+05; Ase+11; Tan+18]

$$m_{\bar{\nu}_e} < 2 \text{ eV} \quad (95\% \text{ C.L.}) .$$

It should be noted, that KATRIN aims for a precision that is better by one order of magnitude.

## 2. The KATRIN Experiment

The KArlsruhe TRItium Neutrino (KATRIN) experiment performs a kinematic measurement of the tritium- $\beta$  spectrum in order to determine the effective mass of the electron antineutrino (from here forth labeled  $m_\nu$ ) as defined by equation (1.13). In case no neutrino mass signal is observed, KATRIN aims to set an upper limit of

$$m_\nu < 200 \text{ meV} \quad (90\% \text{ C.L.}),$$

which is one order of magnitude lower than the one set by its predecessor experiments. KATRIN recorded the first  $\beta$  spectrum in March 2018 and started neutrino mass measurements in March 2019.

This chapter provides an overview of the KATRIN experiment: Section 2.1 lists KATRIN's hardware components and their purpose. Section 2.2 derives a mathematical model of a KATRIN neutrino mass measurement. And section 2.3 presents how such a measurement appears in practice.

### 2.1. Experimental Setup

This section describes the KATRIN apparatus. However, given KATRIN's complexity, it can by no means be exhaustive and for a comprehensive treatise the reader is referred to the KATRIN Design Report [Ang+05] supplemented by an up-to-date hardware overview that is in the making at the time of writing this thesis<sup>1</sup> [Proper Footnote].

ToDo

The KATRIN experiment comprises a 70-m-long beam line depicted in figure 2.1. It can be divided into two sections:

1. Within the **source and transport section (STS)** the tritium decays and the  $\beta$  electrons are magnetically guided along the beam line. Furthermore, the gas flow from the tritium source to the exit of the STS is reduced by 14 orders of magnitude.
2. In the **spectrometer and detector section (SDS)** the  $\beta$  electrons are filtered according to their kinetic energy and finally counted at the detector.

The  $\beta$  electrons must be guided from their point of origin to the detector. Therefore, a magnetic field is created by superconducting coils surrounding the beam line in the STS as well as coils around the spectrometer tank in the SDS. The field lines are parallel to the beam line and intersperse it over the range of the whole experiment. The volume that is mapped onto the detector by this mechanism is called the flux tube. Within the flux tube, charged particles perform cyclotron motions around the field lines and are adiabatically guided from the STS to the detector. Adiabaticity is guaranteed by avoiding strongly varying field strengths on short distances.

---

<sup>1</sup>What to I put here?

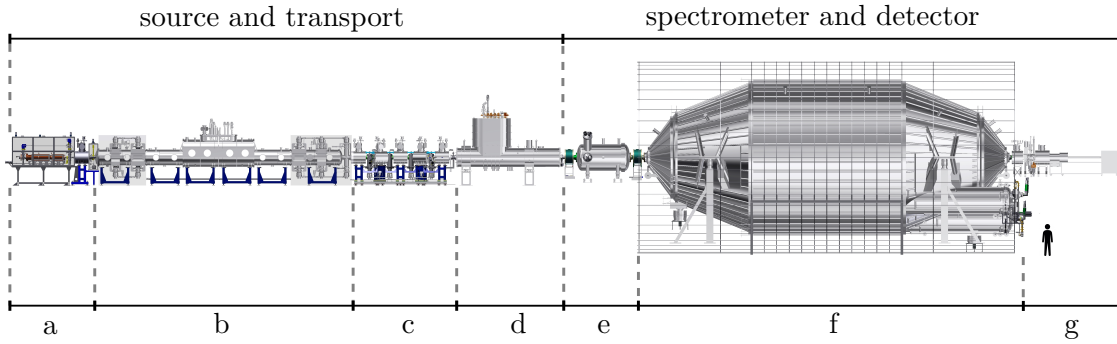


**Figure 2.1.: The KATRIN beamline.** Shown are main hardware components:

- a) rear section (see section 2.1.2)
- b) windowless gaseous tritium source (WGTS) (see section 2.1.1)
- c) differential pumping section (DPS) (see section 2.1.3)
- d) cryogenic pumping section (CPS) (see section 2.1.4)
- e) pre spectrometer (see section 2.1.5)
- f) main spectrometer (see section 2.1.5)
- g) detector (see section 2.1.6)

As  $\beta$  electrons must not lose energy before their detection, the SDS is windowlessly connected to the STS. However, the spectrometer must be kept practically free of any tritium flow for safety reasons and to keep the strict background requirements. Therefore, pumping systems reduce the gas inlet pressure of  $\sim 3 \times 10^{-3}$  mbar to the tritium partial pressure of  $\sim 1 \times 10^{-11}$  mbar of the spectrometer.

The following sections step through the various components along the KATRIN beam line describing their functionality and purpose.

### 2.1.1. Windowless Gaseous Tritium Source

The windowless gaseous tritium source (WGTS) is a 16-m-long, 1.5-m-wide and 4-m-high cryostat. It is depicted in figure 2.2 and a detailed description can e. g. be found in [GB+08]. In the following the major features of the WGTS are reviewed:

**Tritium purity:** The molecular tritium ( $T_2$ ) is injected in the middle of the 10-m beam tube of 90 mm diameter, where it decays. The design gas column density is

$$\rho d = 5 \times 10^{17} \text{ molecules/cm}^2 \quad (2.1)$$

with an isotropic tritium purity of

$$\epsilon_T = 95\%. \quad (2.2)$$

At the front and rear of the WGTS, the gas is extracted from the beam tube by turbo molecular pumps in designated differential pumping sections called DPS-1-R (rear) and DPS-1-F (front). The extracted gas is re-injected in the center of the beam tube. The respective pipe system is called the inner loop [PSB15]. The tritium purity  $\epsilon_T$  must be kept stable on a 0.1 % level [Ang+05]. Therefore, a permeator is installed that separates impurities (like e. g. helium) and ejects them into the exhaust loop of the Tritium Laboratory Karlsruhe (TLK). Furthermore, the isotopic composition of the gas is monitored by a designated laser Raman system (LARA) [Sch13].

**Injection pressure:** The design injection pressure of the tritium gas is 1.8 mbar/s. It must be kept stable at the 0.1 % level. This is achieved via a pressure- and temperature-controlled buffer vessel within the inner loop [PSB15].

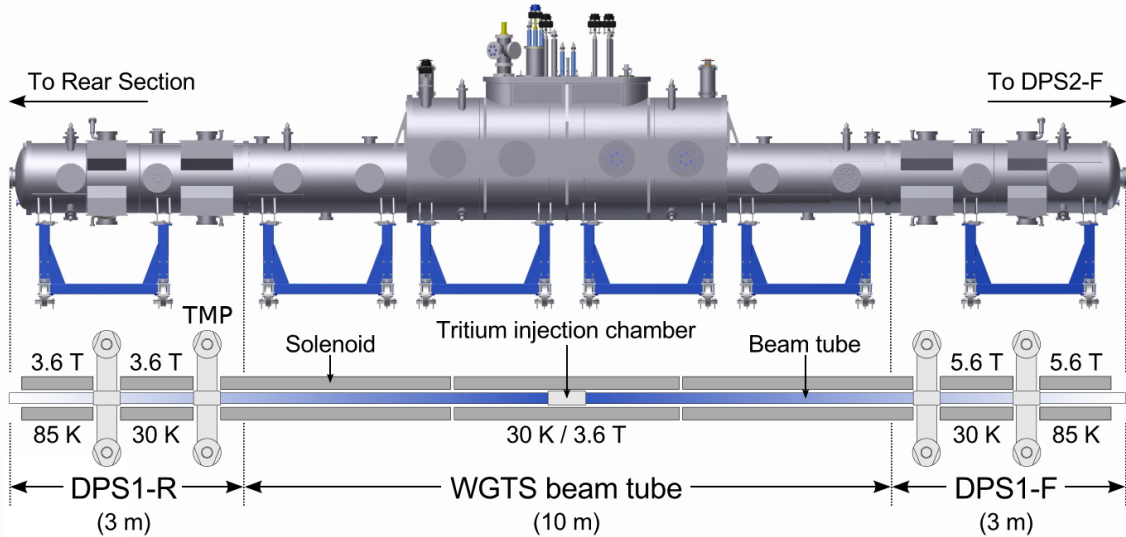


**Figure 2.2.: The windowless gaseous tritium source (WGTS).** The hull and a sketch of the beam tube are shown. Indicated are the 8 turbo molecular pumps (TMP), the 7 magnets, the design temperatures for tritium operation, the maximum magnetic field strengths and a gradient within the beam tube depicting the decreasing gas density from the center to the sides. (Adapted from [Har15].)

**Magnetic field:** In order to adiabatically guide the  $\beta$  electrons to the spectrometer section the WGTS is submerged in a magnetic field parallel to its beam tube of up to 5.6 T. It is created by 7 superconducting coils, that surround the beam tube. These magnets are kept at a temperature of 4.2 K by liquid helium [AB+18].

**Temperature:** On the one hand, thermal motion smears the energy spectrum of the  $\beta$  electrons (Doppler effect). On the other hand, at low temperatures the gas molecules cluster.  $T = 30\text{ K}$  is chosen as a compromise and established by a two-phase neon cooling system. For calibration purposes, it is also possible to operate the WGTS with krypton-83m instead of tritium. This requires a beam tube temperature of  $T = 100\text{ K}$  in order for the krypton not to freeze. In this operational mode the neon has to be exchanged for argon [Ang+05].

### 2.1.2. Rear Section

The rear section terminates the beam line in the upstream direction and houses monitoring, calibration and control devices. It is depicted in figure 2.3 and a detailed description can e. g. be found in [Bab14]. In the following the major features of the rear section are reviewed:

**Electron gun:** The rear section houses an electron gun in order to measure the response function of the experiment (see section 2.2.7) via a electron source with a well-defined energy resolution of  $\sim 0.2\text{ eV}$  and angular resolution of  $\sim 4^\circ$ . The electrons are guided towards and through the rear wall by a designated electromagnetic guidance system. Furthermore, their flight path can be adjusted by dipole magnets mounted in the WGTS which enables a scanning of the full flux tube [Bab14].

**Rear wall and plasma control:** The so-called rear wall is a gold-coated stainless-steel disc with a diameter of 6 inches that terminates the beam tube. It has a hole in the center to let electrons from the electron gun pass through. Its main purpose is the control of plasma effects: Space charges, respectively a plasma, forms within the WGTS due to the tritium decay. Therefore,  $\beta$  electrons may start at different potentials which adds uncertainty to the measured  $\beta$  spectrum. Simulations show that the plasma can be influenced by the rear wall potential which can be controlled via a voltage supply in the range of  $\pm 10\text{ V}$ . Moreover,

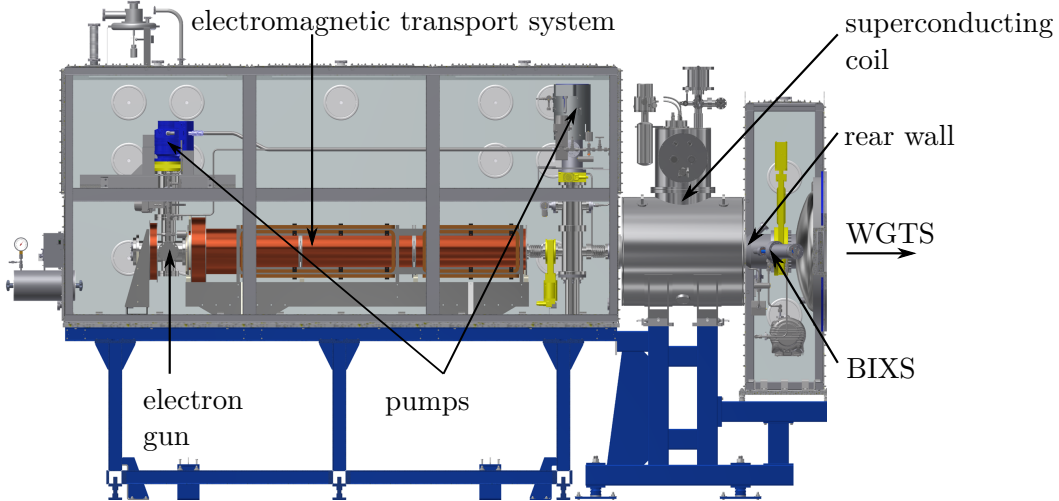


**Figure 2.3.: The rear section** terminates the KATRIN beam line and houses several monitoring and calibration devices that are described in the main text. (Adapted from [Sei19].)

a UV light illumination of the rear wall can extract electrons via the photoelectric effect that can compensate space charges. Therefore, a homogeneous work function of the rear wall with fluctuations less than 20 meV is required [KH+18; Kuc16].

**Activity monitoring:** A super conducting coil designed to create a magnetic field of 4.7 T in the rear section ensures that the magnetic flux tube terminates at the rear wall. Hence, per design of the magnetic guidance,  $\beta$  electrons either arrive at the detector or hit the rear wall. On hitting the rear wall they emit bremsstrahlung. Two dedicated beta-induced X-ray spectroscopy (BIXS) systems measure the corresponding X-ray spectrum to determine the source strength respectively the gas column density, equation (2.1) [Röl15].

### 2.1.3. Differential Pumping Section

The differential pumping section (DPS) is composed of 5 approximately 1-m-long elements. It is depicted in figure 2.4 and a detailed description can e.g. be found in [Kos12]. For orientation, in this section, the elements are labeled 1 to 5 from WGTS to cryogenic pumping section (CPS). In the following the major features of the differential pumping section (DPS) are reviewed:

**Reduction of tritium flow:** The differential pumping section (DPS) consists of 5 beam tube elements that form a  $20^\circ$  angle to each other and are arranged in a chicane.  $\beta$  electrons are magnetically guided along the chicane by a magnetic field of up to 5.5 T created by five superconducting solenoids. Contrarily, the neutral gas molecules scatter off the walls. This reduces the molecular beaming effect and enhances the pumping probability [12]. 4 turbo molecular pumps mounted between the beam tube elements then reduce the gas flow by approximately 5 orders of magnitude and feed the gas into the so-called outer loop where it is reprocessed [Kos12].

**Ion blocking:** In the WGTS, ions such as  $\text{HeT}^+$ ,  $\text{T}_2^+$ ,  $\text{T}_3^+$ ,  $\text{T}_5^+$  can form. If not blocked, they reach the spectrometer section analogously to the electrons which would eventually lead to an increased background rate. A potential barrier created by two ring electrodes in element 5 and the pump port between DPS and CPS set to +100 V avoids this. The positive ions are deflected, and dipole electrodes in the elements 1 to 4 make them drift out of the flux tube. They hit the wall and get neutralized [Kle19].

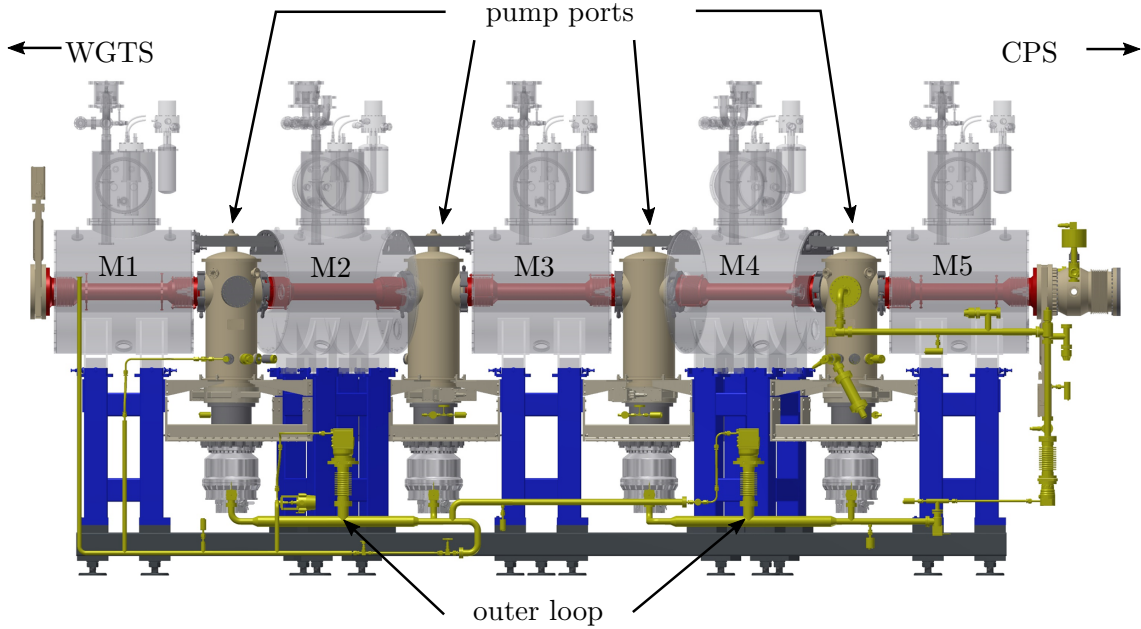


**Figure 2.4.: The differential pumping section (DPS)** reduces the gas flow by 5 orders of magnitude and blocks tritium ions. Its 5 elements, each with a separate magnet (M1-M5), and connected by pump ports, are shown. The outer loop connects the turbo molecular pumps to the infrastructure of the TLK. (Adapted from [Sei19].)

**Ion monitoring:** Downstream of the blocking electrodes the remaining ion flux is measured by a Fourier transform ion cyclotron resonance device (FT-ICR) [UR+09].

#### 2.1.4. Cryogenic Pumping Section

The cryogenic pumping section (CPS) is an approximately 7-m-long cryostat. It is depicted in figure 2.5 and a detailed description can e. g. be found in [Jan15]. For orientation, in this section, its 7 elements are labeled 1 to 7 from WGTS to CPS. In the following the major features of the CPS are reviewed:

**Reduction of tritium flow:** The CPS consists of 7 beam tube elements of which the first 5 are arranged in a similar manner as the beam tube elements of the DPS, in a chicane forming  $15^\circ$  angles. Charged particles are guided along the chicane by a magnetic field of up to 5.6 T created by 7 superconducting coils. Neutral molecules hit the walls that are covered by a frozen argon layer cooled down to 3 K in order to cold-trap particles. These low temperature are achieved via a liquid helium cooling and a heat shield of liquid neon. After the accumulation of about 1 Ci of tritium the argon frost layer has to be renewed. In order to achieve this, the beam tube is warmed up and the argon is pumped off along with the accumulated tritium. Tests and simulations show a reduction of the tritium flow by approximately 10 orders of magnitude [Jan15].

**The forward beam monitor (FBM):** The FBM can be moved horizontally into the pump port between beam tube element 6 and 7 of the CPS with a 2-dimensional spatial resolution of 0.1 mm. Two *pin*-diodes measure the  $\beta$ -electron flux and thus the stability of the column density, equation (2.1). Furthermore, the forward beam monitor (FBM) equips a temperature and a hall sensor. A second detector board holding a Faraday cup for ion measurements is also available [Kle19]. More information about the FBM can e. g. be found in [EH+17].

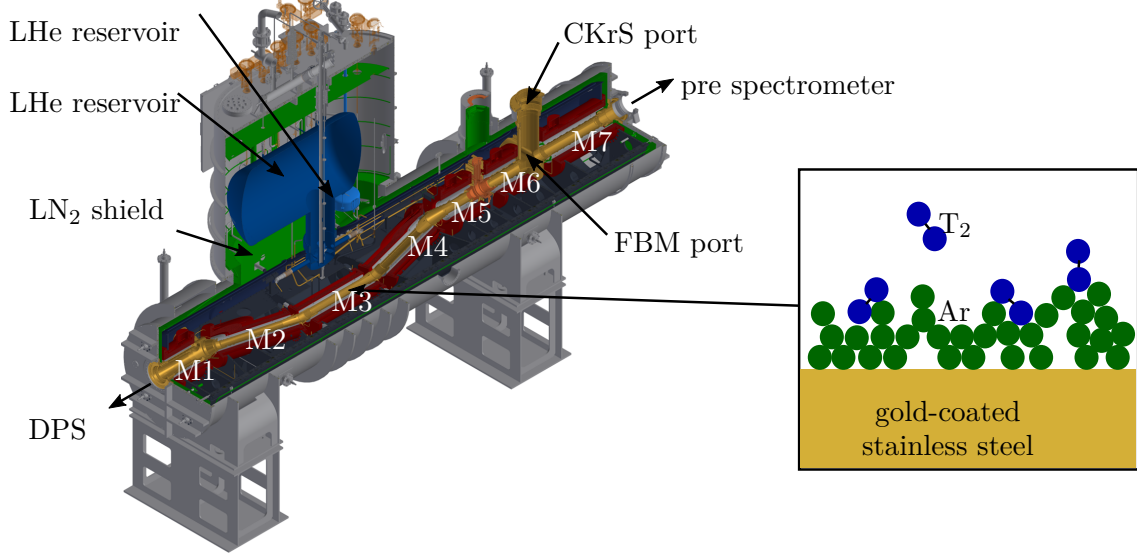


**Figure 2.5.: The cryogenic pumping section (CPS)** is the coldest part of the KATRIN experiment. It consists of 7 elements, labeled from 1 to 7 from the DPS to the pre spectrometer. Elements 2 to 5 are covered by a frozen argon layer at 3 K in order to cold-trap tritium molecules. The low temperatures are established using liquid helium (LHe) and an insulation of liquid nitrogen (LN<sub>2</sub>). Each element is enclosed by a super conducting coil (M1 to M7) for magnetic guidance of the  $\beta$  electrons. For the FBM and CKrS the reader is referred to the main text. (Adapted from [Sei19].)

**The condensed  $^{83m}\text{Kr}$  source (CKrS):** The condensed  $^{83m}\text{Kr}$  source (CKrS) is a sub mono-layer of  $^{83m}\text{Kr}$  on a pyrolytic graphite substrate with a diameter of 2 cm. It can be lowered in the pump port of the CPS and moved in a 2-dimensional plane perpendicular to the beam line. This enables the spatial scanning of the properties of the spectrometer using quasi-monoenergetic conversion electron lines of  $^{83m}\text{Kr}$  [Bau14; Dyb19].

### 2.1.5. Pre and Main Spectrometer

The pre and main spectrometer are vacuum vessels designed to filter passing electrons according to their kinetic energy. The pre spectrometer has a length of 3.4 m and a diameter of 1.7 m. Details on its design can e.g. be found in [PR+12]. The main spectrometer has a length of 23 m and a diameter of 10 m. Details on its design can e.g. be found in [Val09]. The pre and main spectrometer apply the so-called magnetic adiabatic collimation with electrostatic filtering (MAC-E) principle [Ang+05]. The two combined concepts are illustrated in figure 2.6 and will be outlined in the following.

**Electrostatic filtering:** A retarding voltage barrier is applied along the beam axis within the spectrometer, reaching its maximum  $U$  at the so-called analyzing plane in the center and dropping off towards the source and the detector. The retarding voltage barrier deflects electrons with kinetic energies below  $eU$ . For higher energies it depends on the electron's angle with respect to the beam line axis whether it can pass the spectrometer or not. [\[cite or refer\]](#)

**ToDo**

**Magnetic collimation:** The electric field gradient of the retarding voltage barrier is parallel to the beam line, but  $\beta$  electrons are emitted in an arbitrary angle. In order to analyze their full kinetic energy, they have to be collimated. This is achieved by a magnetic field gradient that drops from  $B_S = 3.6\text{ T}$  in the STS to  $B_A \approx 3 \times 10^{-4}\text{ T}$  in the analyzing plane. In the following a plausibility argument for this according to [Zub11] is given: Electrons entering the spectrometer vessel perform cyclotron motions around the

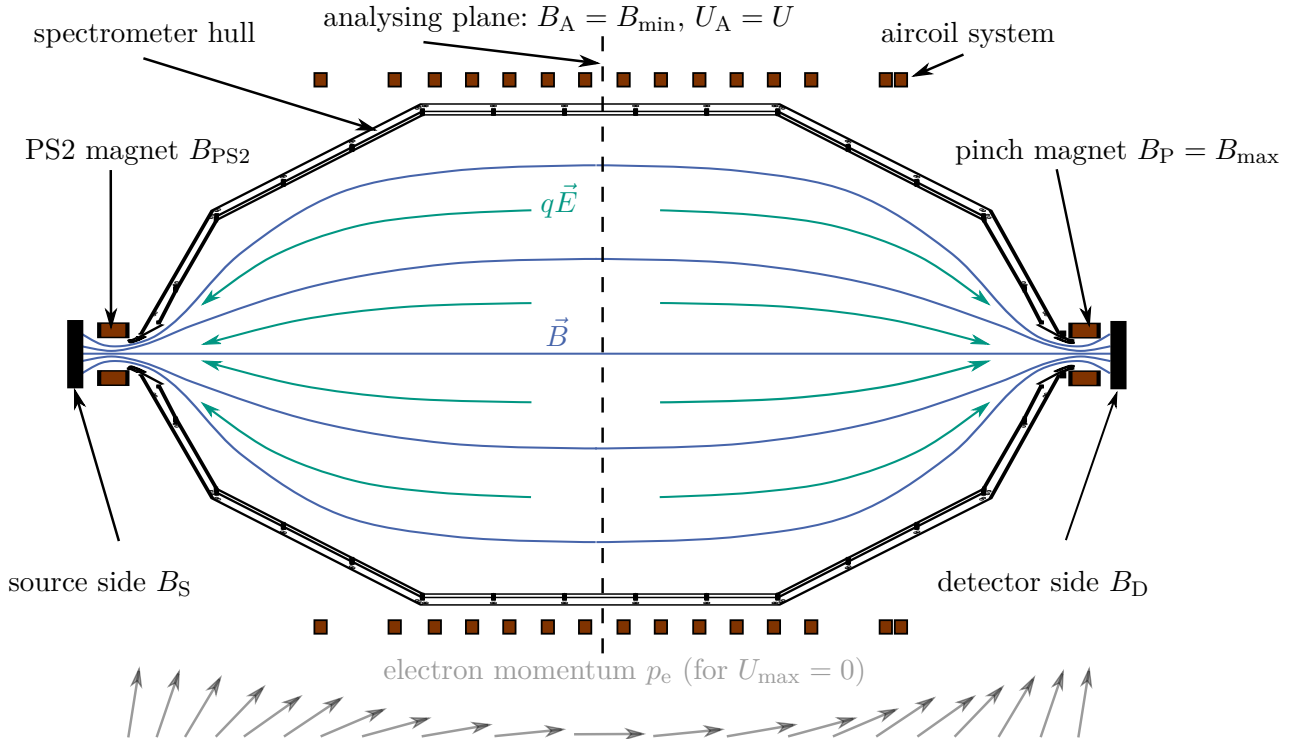


**Figure 2.6.:** Scheme of the KATRIN main spectrometer and the magnetic adiabatic collimation with electrostatic filtering (MAC-E) filter principle. The KATRIN design magnetic field settings are  $B_{PS2} = 4.5$  T,  $B_S = 3.6$  T,  $B_{\max} = 6.0$  T,  $B_D = 3.6$  T,  $B_A \approx 3 \times 10^{-4}$  T.  $\vec{E}$  denotes the magnetic field regulated by the retarding potential  $U$  that reaches its maximum  $U_a = U$  at the analyzing plane. (Adapted from [Sei19].)

magnetic field lines. Their total kinetic energy  $E_S$  is split into a longitudinal component  $E_{\parallel}$  along the beam axis and a transverse component  $E_{\perp}$

$$E_S = E_{\parallel} + E_{\perp}. \quad (2.3)$$

In the non-relativistic and adiabatic approximation the transverse component can be expressed by the magnetic field strength  $B$  and the electron's magnetic moment  $\mu$  respectively its charge  $q = e$ , its mass  $m_e$  and angular momentum  $L$  [Zub11]

$$E_{\perp} = -\mu B = \frac{e}{2m_e} LB. \quad (2.4)$$

Adiabaticity conserves angular momentum  $L$  and the total energy of the electron  $E_S$ . Hence, when the magnetic field strength  $B$  decreases to  $B_A = B_{\min}$  in the analyzing plane, the transverse component of the electron's energy  $E_{\perp}$  decreases likewise and transforms to longitudinal energy  $E_{\parallel}$ .

**Magnetic Bottle effect:** As the source is placed in a lower magnetic field  $B_S$  as the maximum field strength along the beam line  $B_{\max}$  at the detector side,  $\beta$  electrons traveling downstream to the detector are subject to the magnetic bottle effect [Ang+05]. They get reflected and travel upstream to the rear wall if their starting angle  $\theta_S$  with respect to the beam line axis surpasses  $\theta_{\max}$  with

$$\sin \theta_{\max} = \sqrt{\frac{B_S}{B_{\max}}}. \quad (2.5)$$

For the KATRIN design values  $B_{\max} = 6 \text{ T}$  and  $B_S = 3.6 \text{ T}$  one obtains  $\theta_{\max} \approx 51^\circ$ . A cutting angle  $\theta_{\max}$  is beneficial because the greater the emission angle of a  $\beta$  electron the larger the distance it travels in the WGTS and the more it is subject to energy losses such as scattering or synchrotron radiation [Ang+05].

**MAC-E-filter width:** Electrons with a kinetic energy below  $qU$  cannot pass the spectrometer. Electrons with a kinetic energy above  $qU + \Delta E$  do pass the spectrometer. Here,  $\Delta E$  denotes the filter width [Ang+05]

$$\Delta E = \frac{B_A}{B_{\max}} E. \quad (2.6)$$

It depends on the the maximum magnetic field strength along the beam line  $B_{\max} = 6 \text{ T}$ , the kinetic energy of  $\beta$  electrons  $E \approx 18.6 \text{ keV}$ , and the field in the magnetic field in the analyzing plane  $B_A \approx 3 \times 10^{-4} \text{ T}$ . Hence, its KATRIN design value is  $\theta_{\max} \approx 0.93 \text{ eV}$ . Electrons with an energy between  $eU$  and  $eU + \Delta E$  pass the potential barrier only with a certain probability. A quantitative description of this so-called transmission probability will be given in section ?? [add section]. However, it can already be deduced, that a larger MAC-E-filter width adds a greater uncertainty to the measurement and thus it should be kept as low as possible.

## ToDo

**Dimensions of the KATRIN spectrometer:** KATRIN's envisaged sensitivity requires a relative MAC-E-filter width of at least  $E/\Delta E = 20000$ , which directly corresponds the ratio of the magnetic fields  $B_{\max}/B_A$  [Ang+05]. Thus  $B_A$  should be chosen as low as possible. However, the lower  $B_A$ , the wider the flux tube that must be governed by the spectrometer vessel. Also, the magnetic field must decrease at a sufficiently slow rate from the spectrometer's entrance to the analyzing plane in order to guarantee adiabaticity, which requires a certain spectrometer length. Dimensions that meet the demands and are feasible for the main spectrometer were found to be a radius of 10 m and a length of 23 m [Ang+05; Val09].

Now, that the requirements on the magnetic and electrostatic fields are outlined, the following two paragraphs review their technical implementation:

**Magnetic field:** The main spectrometer is surrounded by a system of coils that creates the MAC-E filter's magnetic field. Upstream, there is the PS2 magnet ( $B_{\max} = 4.5 \text{ T}$ ); downstream the pinch ( $B_P = B_{\max} = 6.0 \text{ T}$ ) as well as the detector magnet ( $B_D = 3.6 \text{ T}$ ), which are superconducting solenoids. The field is fine-tuned by a system of air coils around the spectrometer hull: There is the earth magnetic field compensation system (EMCS) with 26 current loops parallel to the beam line axis. Furthermore, there is the low-field correction system (LFCS) with 14 air coils perpendicular to the beam line axis. The combined system constrains the electrons' flux tube to the spectrometer vessel and compensates the Earth's magnetic field as well as effects from ferromagnetic materials in the spectrometer's surroundings [EB+18]. Additionally, a vertical and radial magnetic measuring system (VMMS and RMMS) are installed outside the spectrometer vessel. The field inside the spectrometer vessel is assessed via samples of these measuring systems combined with simulations [LH+18].

**Electrostatic field:** A high-voltage system establishes the MAC-E filter's retarding potential. The retarding voltage's fluctuations must have a standard deviation smaller than 60 mV for the envisaged sensitivity on the neutrino mass [Ang+05]. The antenna-like beam line setup is sensitive to electromagnetic fluctuations of any source, which is why an active so-called post-regulation system is deployed. It monitors the retarding potential and regulates it with the required precision. For the monitoring exist the so-called monitor spectrometer and a voltage divider. For details on the later systems the reader is referred to [TM+09] and [EB+14].

**Background rate:** The KATRIN sensitivity goal requires a background rate of less than 10 mHz [Ang+05]. Several background-related aspects are:

- Vacuum: The spectrometers are operated at a pressure on the order of  $1 \times 10^{-11}$  mbar to  $1 \times 10^{-12}$  mbar. This prevents electron scattering on residual gas and minimizes background effects by ionization. Correspondingly, turbo molecular and getter pumps are installed at three pump ports of the spectrometer vessels. Furthermore, the spectrometers can be baked out at up to 350 °C [AB+16].
- Wire electrodes: The inner walls of the spectrometer vessels are lined by wire electrodes. Their potential is at a few hundred volts more negative than the spectrometer hull reflecting electrons coming from the vessel walls. These electrons may be induced by cosmic rays [Val09].
- Ion blocking: Analogously to the ones in the CPS (section ??), three blocking electrodes are installed; one between the CPS and the pre spectrometer, one between the pre and main spectrometer; and one between the main spectrometer and the detector [Kle19].
- Tandem setup:  $\beta$  electrons may scatter on residual gas or [\[Was war nochmal das andere?\]](#) ToDo. This can either directly lead to secondary electrons or create positive ions that travel down the beam line. The positive ions in turn may again yield secondary electrons through scattering. The more  $\beta$  electrons enter the main spectrometer, the higher is the probability to create secondary electrons. In order to reduce the flux of  $\beta$  electrons into the main spectrometer, the retarding potential of the pre spectrometer is set to a few hundred volts more positive than the one of the main spectrometer. On the one hand this is a countermeasure against background events, but on the other hand, charged particles can be trapped between the two spectrometers due to the electromagnetic setup (Penning trap). A sudden discharge may harm the hardware, especially the detector. Therefore, it is possible to sweep a charged wire through the volume in order to collect the trapped particles and avoid this “Penning discharges” [Val09].

### 2.1.6. Detector Section

The detector section terminates the beam line in downstream direction. It can be separated from the spectrometer section by closing a gate valve. The detector section is depicted in figure 2.7 and a detailed description can e.g. be found in [AB+15]. In the following the major features of the detector section are reviewed:

**Focal plane detector (FPD):** The FPD counts the  $\beta$  electrons that pass the spectrometer section. It is a pin-silicon detector with a sensitive area of 9 cm diameter. It is subdivided in 148 pixels of the same area arranged in 12 rings of 12 pixels each and the so called bull’s eye of 4 pixels in the center. This arrangement allows later correction for radial electrical, magnetic and gas dynamical inhomogeneities in the beam line [AB+15].

**Shield and veto system:** The FPD system’s radiation shield consists of two nested cylindrical shells: an outer lead shell of 3 cm that reduces photon background and an inner copper shell of 1.27 cm that blocks X-rays originating from the outer lead shell. The shield is surrounded by a veto system to tag incoming muons. Such a system is necessary to keep the strict background requirements [AB+15].

**Calibration:** Photoelectron sources can be lowered in the detectors line of sight. The corresponding photocurrent can be measured with the so-called precision ultra-low current integrating normalization electrometer for low-level analysis (PULCINELLA) system. A

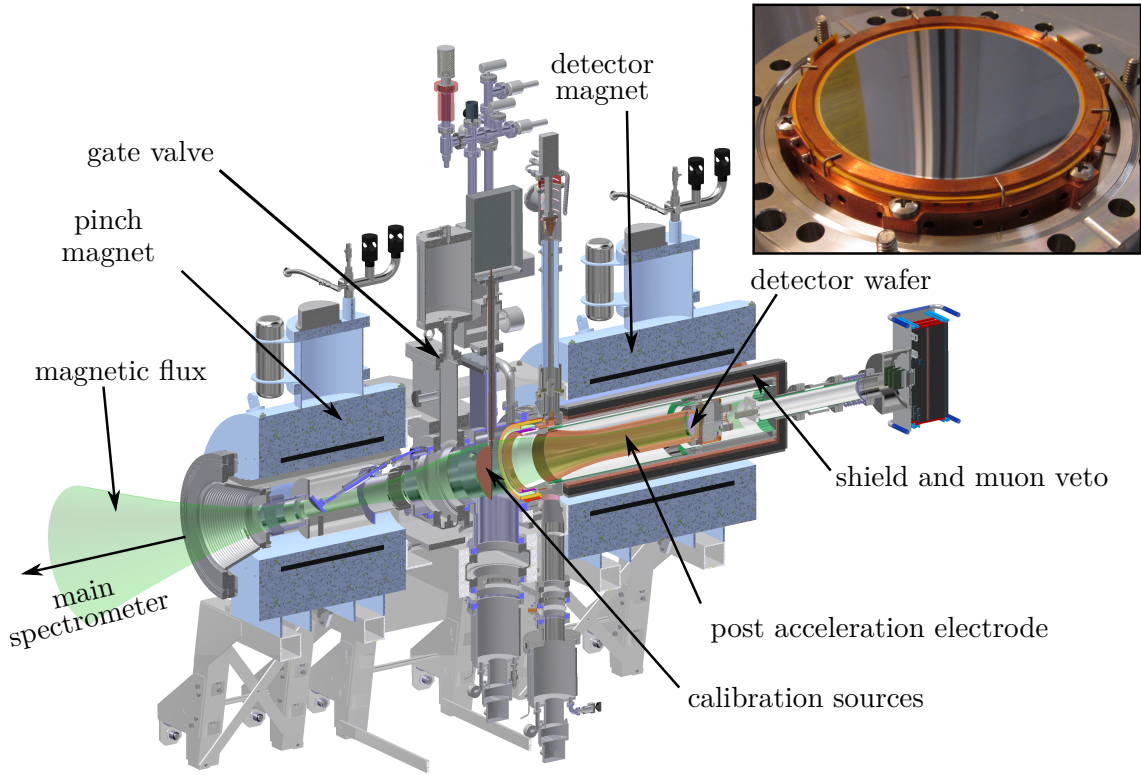


**Figure 2.7.: The detector section** terminates the KATRIN beam line. Among other instruments it houses the focal plane detector (FPD) for  $\beta$  electrons with the detector wafer at its core. For an explanation of the other components the reader is referred to the main text. (Adapted from [Sei19].)

comparison of PULCINELLA and the FPD yields the FPD's detection efficiency. It was determined to be  $\epsilon_{\text{det}} = 95 \pm 1.8 \pm 2.2\%$  [AB+15].

**Detector magnet:** The detector magnet ( $B_D = 3.6$  T) allows to form the flux tube near the detector independently of the main spectrometer magnetic field setting [AB+15].

**Post-acceleration electrode** allows to shift the energy of  $\beta$  electrons arriving from the main spectrometer. This way  $\beta$  electrons can be distinguished from background electrons originating in the detector section by an energy region of interest cut. An appropriate setting was found to be  $\sim 10$  keV [AB+15].

## 2.2. THIS SECTION IS NOT YET STRUCTURED! The Integrated $\beta$ -Decay Spectrum Measured by KATRIN

An analytic description for the electron rate measured by the FPD can be derived. The derivation mostly follows [KB+19; Gro15; Kle14] or is extracted from current production code [KAT19]. The formulas are implemented in the so-called source and spectrum calculation (SSC) software framework.

### 2.2.1. $\beta$ Decay Spectrum

In  $\beta^-$  decay the released energy is distributed among the emitted electron and the anti-electron neutrino. The differential decay rate of a tritium molecule can be described using

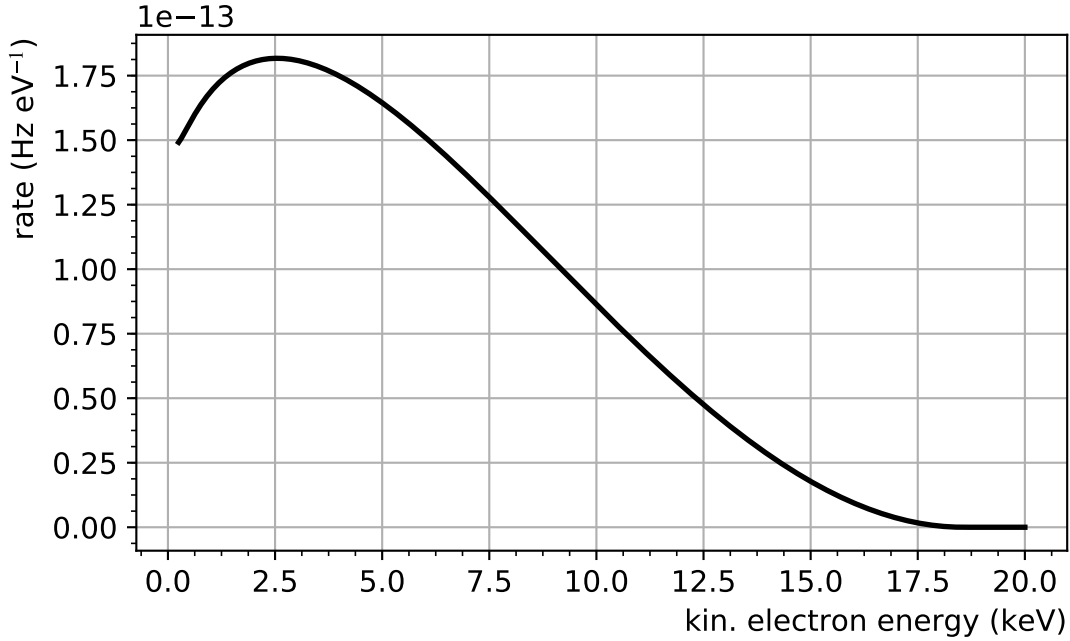


**Figure 2.8.: The  $\beta$  decay spectrum of a tritium molecule as calculated by SSC.**

Fermi theory and Fermi's golden rule as

$$\left( \frac{d\Gamma}{dE} \right) = \frac{G_F^2 |V_{ud}|^2}{2\pi^3} |M_{\text{nuc}}|^2 \cdot F(Z, E) \cdot p(E + m_e) \cdot \sum_{f,i} P_f |U_{ei}|^2 \epsilon_f \sqrt{\epsilon_f^2 - m_i^2} \cdot \Theta(\epsilon_f - m_i) \quad (2.7)$$

It is depicted in figure 2.8. Its constituents are the kinetic electron energy  $E$ ; the PMNS matrix  $U$  (1.4); the neutrino eigenmasses  $m_i$  (1.13); the Fermi constant  $G_F$ ; the up-down-quark-coupling given by the Cabibo angle  $\theta_C$

$$V_{ud} = \cos \theta_C = 0.97425 \pm 0.00022; \quad (2.8)$$

and the nuclear transition matrix element

$$M_{\text{nuc}} = g_V^2 + 3g_A^2 \quad \text{with } g_V = 1 \quad \text{and} \quad g_A/g_V = -1.2646 \pm 0.0035 \quad (2.9)$$

which is independent of the electron's kinetic energy as the decay is super-allowed and given by the vector  $g_V$  and axial vector  $g_A$  coupling.

Furthermore, the Fermi function  $F(Z, E)$  accounts for the Coulomb interaction between the outgoing electron and the daughter nucleus with atomic charge  $Z = 2$  which in its relativistic version can be approximated as

$$F(Z, E) \approx \frac{2\pi\eta}{1 - \exp 2\pi\eta} \cdot R \quad (2.10)$$

with Sommerfeld parameter  $\eta = \alpha Z/\beta$ , fine structure constant  $\alpha$ , relativistic velocity  $\beta$  and a relativistic correction factor  $R = 1.002037 - 0.001427\beta$ .

The phase-space factor of the outgoing electron with momentum  $p$  and mass  $m_e$  is given by the factor  $p(E + m_e)$ .

The phase space factor of the emitted neutrino is described in dependence of the following quantities: total nuclear tritium decay energy  $Q$  (mass difference of mother and daughter nucleus) corrected for the nucleus recoil  $E_{\text{rec}}$  also called endpoint of the  $\beta$  spectrum

$$E_0 = Q - E_{\text{rec}}; \quad (2.11)$$

the kinetic electron energy  $E$  and the final state energy of the molecular system  $V_f$ . The probability that the molecular system is in a final state of energy  $V_f$  after the decay is denoted by  $P_f$ . Then the energy of the neutrino reads

$$\epsilon_f = E_0 - E - V_f. \quad (2.12)$$

The excited energy state  $f$  is caused by vibration, rotation or electronic excitation of the decaying molecule. Details and tabulated values can e.g. be found in [BPR15] and references therein.

The neutrino's momentum is  $\sqrt{\epsilon_f^2 - m_i^2}$ , where  $m_i$  denotes one of the neutrino eigenmasses. The complete phase space factor of the neutrino is a sum over all possible molecular final states labeled  $f$  and neutrino eigenmasses labeled  $i$ .

Lastly, the Heavyside step function  $\Theta$  ensures a positive kinetic energy of the neutrino.

### 2.2.2. Detector Counts

The KATRIN detector counts electrons. The  $\beta$  electrons are adiabatically guided from the WGTS to the detector by magnetic fields. The magnetic field lines are parallel to the beam line axis. The angle between the flight direction of a  $\beta$  electron and the beam line axis towards the detector is denoted by the pitch angle  $\theta \in [0^\circ, 180^\circ]$ . The starting position of an  $\beta$  electron is denoted by its 1-dimensional coordinate along the beam line axis  $z_S$ .

KATRIN measures an integrated  $\beta$  spectrum. In other words, the detector counts electrons of kinetic energy  $E_S$  above a threshold, the so-called retarding energy  $qU$ . The integrated  $\beta$  spectrum can be scanned by varying  $qU$ .

A  $\beta$  electron emitted in the WGTS reaches the detector with a probability modeled by the so-called response function  $R$  (see section 2.2.7).  $R$  depends on the experimental settings (such as the electromagnetic fields and the gas dynamics) and especially on the retarding energy  $qU$ . Here,  $R$  denotes the transmission probability for a  $\beta$  electron of a fixed starting kinetic energy  $E_S$ , starting position  $z_S$  and starting pitch angle  $\theta_S$ . The probability of a  $\beta$  electron for being counted when reaching the detector is denoted by the detection efficiency  $\epsilon_{\text{det}}$ . Furthermore, the number of tritium molecules in the WGTS in a small area around the coordinate  $z$  is denoted by  $dN_T(z)$ .

Then, the measured integrated rate is expressed as integral from the threshold energy  $qU$  to the endpoint energy  $E_0$  (2.11) over the differential rate  $d\Gamma / dE_S$  (2.7) weighted with the probability given by  $R$  as

$$\Gamma(qU, z_S, \theta_S) = \epsilon_{\text{det}} \cdot dN_T(z_S) \cdot \int_{qU}^{E_0} \left( \frac{d\Gamma(E_S)}{dE_S} \right) \cdot R(E_S, qU, z_S, \theta_S) dE_S, \quad (2.13)$$

which eventually leads to  $\beta$  electron counts by multiplication with the measurement time  $t(qU)$  at a retarding energy  $qU$

$$N(qU, z_S, \theta_S) = \Gamma(qU, z_S, \theta_S) \cdot t(qU). \quad (2.14)$$

### 2.2.3. Discretization of the WGTS Volume

The counts  $N$  (2.14) are given for  $\beta$  electrons of a fixed starting position  $z_S$ . All starting positions  $z_S \in [-L/2, +L/2]$  within the WGTS of length  $L$  contribute to the total count rate at the detector. Integrating along the beam axis accounts for this

$$N(qU, \theta_S) = \int_{-L/2}^{+L/2} \frac{dN(qU, \theta_S, z_S)}{dz_S} dz_S \quad (2.15)$$

Numerically, the same result can be obtained by a sufficiently fine discretization of the WGTS volume into  $S$  slices. The counts  $N$  (2.14) are adapted accordingly to account for discrete starting  $\beta$  electron positions  $z_S^j$

$$N(qU, \theta_S, z_S) \rightarrow N^j(qU, \theta_S, z_S^j) \equiv N^j(qU, \theta_S). \quad (2.16)$$

Then, the total counts read

$$N(qU, \theta_S) = \sum_{j=1}^S N^j(qU, \theta_S). \quad (2.17)$$

Within this chapter, from here forth all quantities that are subject to discretization will be labeled with an upper index  $j$ . The discretization especially propagates to the response function  $R \rightarrow R^j$  and its constituents.

### 2.2.4. Magnetic Bottle Effect

The  $\beta$  electrons are adiabatically guided to the detector by magnetic fields. The magnetic field strength at the starting position of a  $\beta$  electron in the WGTS is denoted by  $B_S^j$ . The maximum magnetic field strength along the beam line is denoted by  $B_{\max}$ . As  $B_S^j < B_{\max}$   $\beta$  electrons travelling downstream to the detector are subject to the magnetic bottle effect. They get reflected and travel upstream to the rear wall if their starting pitch angle  $\theta_S$  surpasses  $\theta_{\max}^j$  with

$$\sin \theta_{\max}^j = \sqrt{\frac{B_S^j}{B_{\max}}}. \quad (2.18)$$

(Its KATRIN design value is  $\theta_{\max} \approx 51^\circ$ .) A cutting angle  $\theta_{\max}^j$  is beneficial because the greater the emission angle of a  $\beta$  electron the larger the distance it travels in the WGTS and the more it is subject to energy losses such as scattering or synchrotron radiation.

### 2.2.5. Scattering Probabilities

The probability for a  $\beta$  electron to reach the detector (the response function  $R^j$ ) depends on the scattering probabilities  $P_l$  ( $l \in \mathbb{N}$ ).  $P_l$  denotes the probability of an electron to scatter  $l$  times when travelling through the WGTS.  $P_l$  depends on the starting position  $z_S$  of a  $\beta$  electron in the WGTS as well as on its starting pitch angle  $\theta_S$ . The expected scattering count for a  $\beta$  electron when travelling through the WGTS is the product of the line density  $\lambda$  the electron passes through and the scattering cross section  $\sigma$

$$\mu(z_S, \theta_S) = \lambda(z_S, \theta_S)\sigma. \quad (2.19)$$

The electron moves on a spiral due to its cyclotron motion. Therefore, when traveling an infinitesimal distance  $dz$  in  $z$ -direction, it travels a total distance of

$$ds = \frac{1}{\cos \theta_S} dz. \quad (2.20)$$

The line density  $\lambda$  can be expressed as a line integral over the gas density  $\rho$  along the electrons path  $\varphi$

$$\lambda(z_S, \theta_S) = \int_{\varphi} \rho(\vec{r}) \, ds. \quad (2.21)$$

Assuming that the gas density  $\rho$  only depends on the  $z$ -position along the beam line and vanishes for  $z > L/2$  (beyond the WGTS) equation (2.21) becomes

$$\lambda(z_S, \theta_S) = \frac{1}{\cos \theta_S} \int_{z_S}^{L/2} \rho(z) \, dz. \quad (2.22)$$

Hence, the expected scattering count (2.19) becomes

$$\mu(z_S, \theta_S) = \frac{\sigma}{\cos \theta_S} \int_{z_S}^{L/2} \rho(z) \, dz. \quad (2.23)$$

The scattering process fulfills the conditions of a Poisson process, namely scattering once does quasi not influence the probability of an electron to scatter again; the expected scattering count  $\mu$  (2.23) stays quasi constant; and it is unlikely for two scatterings to happen within a short distance. Thus, the probability for  $l$ -fold scattering can be expressed as a Poisson distribution

$$P_l(z_S, \theta_S) = \frac{\mu(z_S, \theta_S)^l}{l!} e^{-\mu(z_S, \theta_S)}. \quad (2.24)$$

### Discretization of the WGTS volume

In the discretized case the WGTS volume is divided into  $S$  slices indexed by  $k$  with an average gas density  $\bar{\rho}^k$ . A slice  $k$  starts at position  $Z_s^k$  and ends at position  $Z_e^k$  with a width of  $W^k = Z_e^k - Z_s^k$ . For  $\beta$  electrons that start at a position  $z$  within slice  $j$  the expected scattering count (2.19) becomes

$$\mu(z_S, \theta_S) \rightarrow \mu^j(z, \theta_S) = \underbrace{\frac{\sigma}{\cos \theta_S} (Z_e^j - z) \bar{\rho}^j}_{(*)} \underbrace{\sum_{k=j+1}^S \bar{\rho}^k W^k}_{(**)}. \quad (2.25)$$

The gas column density in front of a  $\beta$  electron is split in two parts: the slice of its origin (\*) and all slices downstream (\*\*).

The Poisson distribution is formed for the expected scattering count  $\mu^j$  (2.25) and averaged over all starting positions within the slice  $j$  which yields the discretized scattering probabilities

$$P_l^j(\theta_S) = \frac{1}{W^j} \int_{Z_s^j}^{Z_e^j} \frac{(\mu^j(z, \theta_S))^l}{l!} e^{-\mu^j(z, \theta_S)} \, dz. \quad (2.26)$$

#### 2.2.6. MAC-E Principle and Transmission Function

The spectrometers of KATRIN follow the magnetic adiabatic collimation with electrostatic filtering (MAC-E) principle. Figure 2.9 shows a corresponding sketch. The main spectrometer is a vacuum vessel with a downstream magnet of strength  $B_{PS2}$  and an upstream magnet of strength  $B_P$  making electrons form a magnetic flux tube. In the case of KATRIN the fluxtube begins in the STS with a magnetic field strength of  $B_S^j$ . In other words, the spectroscopic properties are not solely determined by the spectrometer vessel, but also by the STS. The minimum magnetic field strength  $B_{min} = B_A$  is reached at the so-called analyzing plane in the vessel center. Electrons entering the vessel perform cyclotron motions

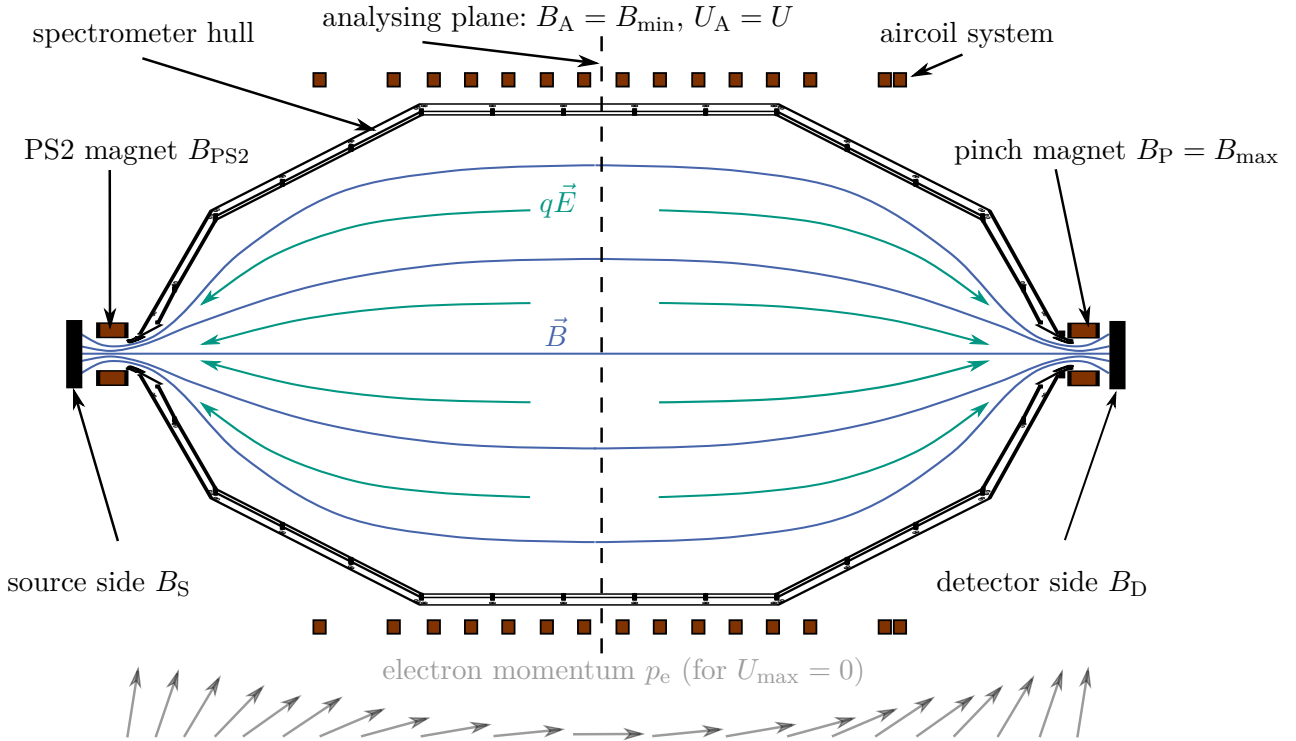


**Figure 2.9.: Scheme of the KATRIN main spectrometer and the magnetic adiabatic collimation with electrostatic filtering (MAC-E) filter principle.** The KATRIN design magnetic field settings are  $B_{PS2} = 4.5 \text{ T}$ ,  $B_S^j = 3.6 \text{ T}$ ,  $B_{\max} = 6.0 \text{ T}$ ,  $B_D = 3.6 \text{ T}$ ,  $B_A \approx 3 \times 10^{-4} \text{ T}$ .  $\vec{E}$  denotes the magnetic field regulated by the retarding potential  $U$  that reaches its maximum  $U_a = U$  at the analyzing plane. (Adapted from [Sei19])

around the magnetic field lines. Their total kinetic energy  $E_S$  is split into a longitudinal component  $E_{\parallel}$  along the beam axis and a transverse component  $E_{\perp}$

$$E_S = E_{\parallel} + E_{\perp}. \quad (2.27)$$

In the non-relativistic and adiabatic approximation the transverse component can be expressed by the magnetic field strength  $B$  and the electron's magnetic moment  $\mu$  respectively its charge  $q = e$ , its mass  $m_e$  and angular momentum  $L$ .

$$E_{\perp} = -\mu B = \frac{e}{2m_e} LB. \quad (2.28)$$

Adiabaticity conserves angular momentum  $L$  and the total energy of the electron  $E_S$ . Hence, when the magnetic field strength  $B$  decreases to  $B_A = B_{\min}$  in the analyzing plane, the transverse component of the electron's energy  $E_{\perp}$  decreases likewise and transforms to longitudinal energy  $E_{\parallel}$ . Additionally, a retarding voltage barrier is applied along the beam axis, reaching its maximum  $U$  at the analyzing plane and dropping off towards the source and the detector. In order to pass through the filter, electrons need a total kinetic energy  $E_S$  greater than the transmission energy  $E_{\text{tr}}^j(qU, E_S, \theta_S)$  that depends on their starting potential  $U_S^j$ , their starting pitch angle  $\theta_S$  and starting Lorentz factor  $\gamma_S$

$$E_{\text{tr}}^j(qU, E_S, \theta_S) = \frac{q(U - U_S^j)}{1 - \sin^2 \theta_S \frac{B_A}{B_S^j} \frac{\gamma_S + 1}{2}}. \quad (2.29)$$

For ease of notation, the dependency on  $B_S^j$ ,  $B_A$  and  $U_S^j$  is left implicit. Note further that the right hand side of (2.29) also depends on the starting energy of a  $\beta$  electron as it depends on  $\gamma_S$ .

Then, the probability for an electron to pass through a MAC-E filter, the so-called transmission function, can be written as

$$\mathcal{T}^j(E_S, qU, \theta_S) = \begin{cases} 1 & \text{if } E_S > E_{\text{tr}}^j(qU, E_S, \theta_S) \\ 0 & \text{otherwise} \end{cases}. \quad (2.30)$$

The transmission condition for the energy  $E_S > E_{\text{tr}}^j(qU, E_S, \theta_S)$  can be reformulated to a condition for the pitch angle  $\theta_S^j$

$$E_S > E_{\text{tr}}^j(qU, E_S, \theta_S) \quad (2.31)$$

$$\Leftrightarrow \theta_S < \theta_{\text{tr}}^j(E_S, qU) := \arcsin \left( \sqrt{\frac{E_S - q(U - U_S^j)}{E_S} \frac{B_A}{B_S^j} \frac{\gamma_S + 1}{2}} \right) \quad (2.32)$$

This allows to rewrite the transmission function (2.30) as

$$\mathcal{T}^j(E_S, qU, \theta_S) = \begin{cases} 1 & \text{if } \theta_S > \theta_{\text{tr}}^j(E_S, qU) \\ 0 & \text{otherwise} \end{cases}. \quad (2.33)$$

### 2.2.7. Response Function

The so-called response function denotes the probability of a  $\beta$  electron emitted in the WGTS with starting energy  $E_S$  and pitch angle  $\theta_S$  to reach the detector when a retarding voltage of  $U$  is applied to the spectrometer. In addition to the transmission function  $\mathcal{T}^j$  (2.31) it incorporates the energy loss  $\epsilon$  of the  $\beta$  electrons due to scattering in the gas in the WGTS. If up to  $N$ -fold scattering is considered, the response function reads

$$R^j(E_S, qU, \theta_S) = \int_0^{E_S} \sum_{l=1}^N \mathcal{T}^j(E_S - \epsilon, qU, \theta_S) \cdot P_l^j(\theta_S) \cdot f_l(\epsilon) d\epsilon. \quad (2.34)$$

Here,  $P_l^j$  (2.26) denotes the probability of a  $\beta$  electron to scatter  $l$  times when travelling through the WGTS.  $f_l(\epsilon)$  is the so-called energy loss function. It denotes the probability for  $\beta$  electrons to loose the energy  $\epsilon$  when scattering  $l$  times. For no scattering the Dirac delta function is used

$$f_0(\epsilon) = \delta(\epsilon). \quad (2.35)$$

For 1-fold scattering  $f_1$  is denoted without index  $f_1 = f$ . For  $l > 1$  and  $l$ -fold scattering  $f_l$  is the  $l$ -fold convolution of  $f$  with itself

$$f_l(\epsilon) = \bigotimes_{i=1}^l f(\epsilon) \quad (2.36)$$

where  $\otimes$  denotes the convolution

$$(f \otimes f)(\epsilon) = \int_0^\infty f(\epsilon - \epsilon') f(\epsilon') d\epsilon'. \quad (2.37)$$

### 2.2.8. Energy Loss Function

The response function (2.34) depends on the energy loss function  $f$ .  $f(\epsilon)$  denotes the probability of a  $\beta$  electron to loose the energy  $\epsilon$  when scattering once on a gas molecule. A review of different models for  $f$  can e.g. be found in [Tro19]. E.g. a phenomenological model fitted to data was established by the Troitsk experiment for tritium [AB+00] as well as for deuterium and hydrogen molecules [AB17]. Currently a corresponding modeling effort is made based on data taken by KATRIN. Details will be discussed in section ??.

### 2.2.9. Distribution of Pitch Angles

The detected counts  $N$  (2.17) are given for a fixed starting pitch angle  $\theta_S$  of  $\beta$  electrons which motivates to average over pitch angles. Any function  $g(\theta_S)$  depending on a fixed pitch angle  $\theta_S$  can be averaged given the distribution  $\omega(\theta_S)$  of  $\theta_S$  and its maximum value  $\theta_{\max}^j$  (2.18) as

$$\langle g(\theta_S) \rangle \equiv \bar{g} = \frac{\int_0^{\theta_{\max}^j} \omega(\theta_S) g(\theta_S) d\theta_S}{\int_0^{\theta_{\max}^j} \omega(\theta_S) d\theta_S}. \quad (2.38)$$

An isotropic  $\beta$  electron emission by a tritium molecule into the unit sphere, meaning all combinations of spherical emission angles ( $\varphi, \vartheta = \theta_S$ ) are equally likely, yields as distribution for their starting pitch angle

$$\omega(\theta_S) = \sin \theta_S \quad (2.39)$$

$$\int_0^{\theta_{\max}^j} \omega(\theta_S) d\theta_S = \frac{1}{1 - \cos \theta_{\max}^j}. \quad (2.40)$$

### Scattering Probabilities

Averaging the scattering probabilities  $P_l^j$  (2.26) yields

$$\bar{P}_l^j = \frac{1}{1 - \cos \theta_{\max}^j} \int_0^{\theta_{\max}^j} P_l^j(\theta_S) \sin \theta_S d\theta_S. \quad (2.41)$$

This expression is helpful when averaging the detected counts  $N$  (2.17) and bringing the corresponding averaged response function in a demonstrative form as shown below.

### Counts and Response Function

The detected counts  $N$  (2.17) depend on the starting pitch angle  $\theta_S$  of the  $\beta$  electrons. They have to be averaged over  $\theta_S$ . The corresponding integral can be swapped with the sum over the WGTS slices and the integral over the energy and propagates to the response term

$$\bar{N}(qU) \propto \sum_{j=1}^S N_T^j \int_{qU}^{E_0} \left( \frac{d\Gamma(E_S)}{dE_S} \right) \cdot \frac{1}{1 - \cos \theta_{\max}^j} \int_0^{\theta_{\max}^j} R^j(E_S, qU, \theta_S) \sin \theta_S d\theta_S dE_S. \quad (2.42)$$

Here  $N_T^j$  denotes the number of tritium molecules in a WGTS slice  $j$ . The response function  $R^j$  (2.34) can be averaged as

$$\begin{aligned} \bar{R}^j(E_S, qU) &= \frac{1}{1 - \cos \theta_{\max}^j} \int_0^{\theta_{\max}^j} R^j(E_S, qU, \theta_S) \sin \theta_S d\theta_S \\ &= \int_0^{E_S} \sum_{l=1}^N \frac{1}{1 - \cos \theta_{\max}^j} \int_0^{\theta_{\max}^j} \mathcal{T}^j(E_S - \epsilon, qU, \theta_S) \cdot P_l^j(\theta_S) \sin \theta_S d\theta_S f_l(\epsilon) d\epsilon. \end{aligned} \quad (2.43)$$

The transmission function  $\mathcal{T}^j$  (2.33) is a step function. Assuming that  $\theta_{\max}^j$  (2.18) is always greater than the transmission angle  $\theta_{\text{tr}}^j$  (2.31), the upper integral boundary changes which yields the averaged response function

$$\bar{R}^j(E_S, qU) = \int_0^{E_S} \sum_{l=1}^N \int_0^{\theta_{\text{tr}}^j(E_S - \epsilon, qU)} \frac{\sin \theta_S \cdot P_l^j(\theta_S)}{1 - \cos \theta_{\max}^j} d\theta_S f_l(\epsilon) d\epsilon. \quad (2.44)$$

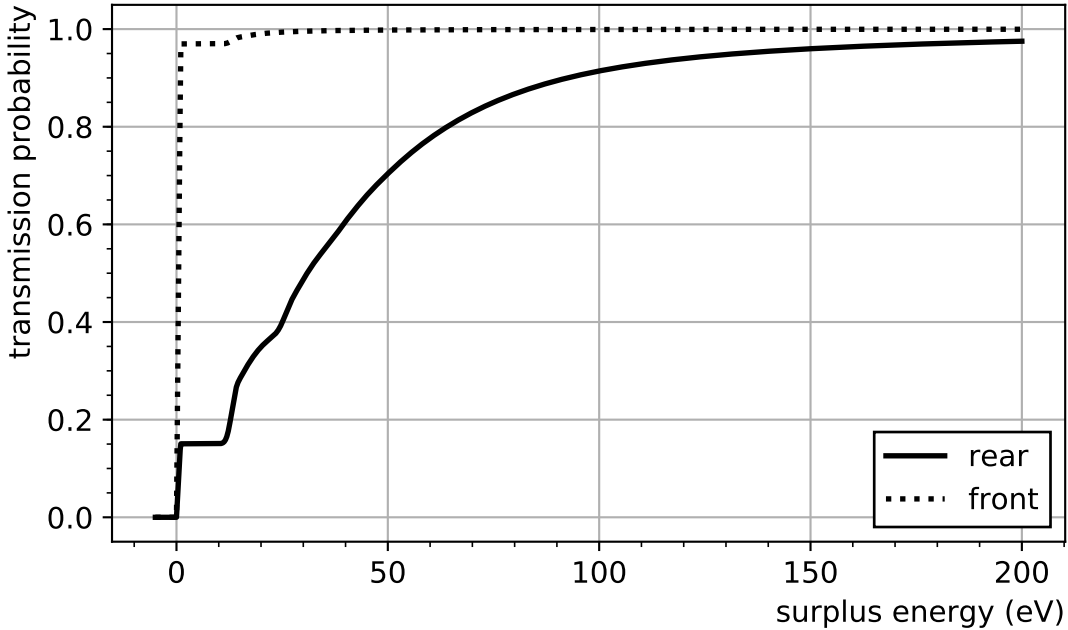


**Figure 2.10.: The response function** as calculated by SSC. The surplus energy denotes the difference between the starting kinetic energy  $E_S$  of a  $\beta$  electron and the retarding energy  $qU$ . The response function  $\bar{R}^j$  (2.46) is depicted for electrons starting at the rear and front of the WGTs.

The averaged response function  $\bar{R}^j$  is depicted in figure 2.10. Its formula (2.44) can be rewritten to match the form of the formula for the non-averaged response function  $R^j$  (2.34). Therefore, the averaged scattering probabilities  $\bar{P}_l^j$  (2.41) are used and the factor  $1 = \bar{P}_l^j / \bar{P}_l^j$  is inserted in equation (2.44):

$$\bar{R}^j(E_S, qU) = \int_0^{E_S} \sum_{l=1}^N \underbrace{\int_0^{\theta_{\text{tr}}^j(E_S - \epsilon, qU)} \frac{\sin \theta_S \cdot P_l^j(\theta_S)}{(1 - \cos \theta_{\max}^j) \cdot \bar{P}_l^j} d\theta_S \cdot \bar{P}_l^j \cdot f_l(\epsilon) d\epsilon}_{T^{j,*}(E_S - \epsilon, qU)} \quad (2.45)$$

$$= \int_0^{E_S} \sum_{l=1}^N T^{j,*}(E_S - \epsilon, qU) \cdot \bar{P}_l^j \cdot f_l(\epsilon) d\epsilon. \quad (2.46)$$

Note that the non-averaged response function  $R^j$  (2.34) has the same form as the averaged one  $\bar{R}^j$  (2.46) if the non-averaged transmission function  $\mathcal{T}^j$  (2.33) is replaced by the modified transmission function  $T^{j,*}$  and the non-averaged scattering probabilities  $P_l^j$  (2.24) by the averaged ones  $\bar{P}_l^j$  (2.41).

Note further that albeit equation (2.44) and equation (2.46) are analytically equal, they are not equal implementation-wise. Currently the implementation of the response function follows equation (2.46). On one hand, equation (2.44) is more “light-weight” as it does not use the averaged scattering probabilities. In the future it might be beneficial to alter the implementation to simplify the program structure and cut down on the number of calculations. On the other hand, equation (2.45) allows the exchange of implementations for the transmission function whereas equation (2.44) only allows to exchange the implementation of the response function as a whole.

### 2.2.10. Reconciliation

The predicted counts for a retarding energy of  $qU$  when measuring a duration  $t(qU)$  are

$$\bar{N}(qU) = t(qU) \cdot \epsilon_{\text{det}} \cdot \left( A_S \cdot \sum_j N_T^j \cdot \int_{qU}^{E_0} \left( \frac{d\Gamma(E_S)}{dE_S} \right) \cdot \bar{R}^j(E_S, qU) dE_S + R_{\text{bg}} \right). \quad (2.47)$$

Here,  $A_S = 1$  is a normalization factor,  $\epsilon_{\text{det}} \in [0, 1]$  is the detector efficiency, the sum goes over all source slices,  $N_T^j$  is the number of tritium molecules in the  $j$ th source slice,  $(d\Gamma(E_S)/dE_S)$  is the differential rate from (2.7),  $\bar{R}^j(E_S, qU)$  is the response function from (2.46) and  $R_{\text{bg}}$  is the rate of background events.

### 2.2.11. Amendments

Equation (2.47) is a scaffold for an analytic model of the counts measured by the KATRIN detector. Modifications of isolated terms can consider further effects. Selected examples are:

- **Doppler effect:** Gas flow and temperature move the tritium molecules and hence, smear the kinetic energy distribution of  $\beta$  electrons. This can be modelled by convolving the differential rate  $d\Gamma/dE$  (2.7) with a Maxwellian distribution or by applying corrections to the final energy states of the decaying molecules.
- **Plasma potential:** Space charges, respectively a plasma, forms within the WGTS due to the tritium decay. Electrons passing through space charges might either gain or loose energy. In a segmented WGTS volume, this is implemented by using an effective retarding energy corrected for the plasma potential  $V^j$  in the slice  $j$

$$qU \rightarrow qU_{\text{eff}}^j = qU - V^j \quad (2.48)$$

when calculating the response function  $\bar{R}^j$  (2.46). Note that this is equivalent to using the starting potential  $U_S^j$  in the transmission energy  $E_{\text{tr}}^j$  (2.29).

- **Further discretization of the WGTS volume:** The SSC software allows to discretize the WGTS not only into slices, but also to subdivide the slices further into rings and the rings into segments. This enables an arbitrary spacial binning for WGTS properties such as the magnetic field or gas density. Then, additionally, the retarding energy  $qU \rightarrow qU^j$ , the maximum magnetic field strength along the beam line  $B_{\max} \rightarrow B_{\max}^j$ , the magnetic field strength in the analyzing plane  $B_A \rightarrow B_A^j$  and the detector efficiency  $\epsilon_{\text{det}} \rightarrow \epsilon_{\text{det}}^j$  become subject to discretization because they exhibit a radial dependency. Furthermore, the WGTS can be subdivided into volumes that map onto a specific detector pixel due to magentic guidance. This enables pixel-wise modelling of electron counts.

## 2.3. A KATRIN Neutrino Mass Measurement

KATRIN measures electron counts as described in (2.47) at a set of retarding energies  $qU_i$ . How much measurement time  $t(qU_i)$  is attributed to a certain retarding energy is called a measurement time distribution (MTD). The MTD influences the experiment's sensitivity to the neutrino mass. An optimal MTD balances the following aspects:

1. Some measurement time has to be attributed to retarding energies beyond the endpoint of the spectrum to determine the background rate. The optimal duration depends on the background rate.
2. The shape of the integral tritium  $\beta$  spectrum depends the strongest on the neutrino mass near its endpoint  $E_0$  (2.11). [\[Ask Hendrik for plot.\]](#)

To Do

3. Measurements deeper into the spectrum increase the count rate and hence, lower the statistical uncertainty due to Poisson statistics.
4. The theoretical description of the integral tritium  $\beta$  spectrum is optimized for the endpoint region. Deeper scans introduce modeling uncertainties.

The KATRIN Design Report [Ang+05] suggests 5 MTDs for different measurement ranges  $[E_0 - \alpha \text{ eV}, E_0 + 5 \text{ eV}]$  with  $\alpha \in \{20, 25, 30, 40, 50\}$  and the conclusion that  $\alpha = 30$  works best for the KATRIN experiment.

Furthermore, searches for sterile neutrinos at the keV-scale would require deeper scans. Also, during commissioning measurement it makes sense to vary the MTD, especially to perform deeper scans, to ensure a comprehensive understanding of the KATRIN apparatus.

Several measurement campaigns were already conducted. The First Tritium (FT) commissioning campaign successfully proved the apparatus functioning. The corresponding MTD covered a range starting at  $\sim E_0 - 1.6 \text{ keV}$ . The KATRIN Neutrino Mass Measurement 1 (KNM1) campaign is evaluated during the writing of this thesis. It set out to establish an unprecedented limit on the neutrino mass by  $\beta$  decay measurements. Its MTD starts at  $\sim E_0 - 90 \text{ eV}$ .

### 3. Statistical Methods and Neutrino Mass Inference at KATRIN

The neutrino mass  $m_\nu$ , alongside with an uncertainty will be retrieved by comparing the output of the KATRIN measurement with theoretical predictions. This process is called parameter inference. There exist different statistical approaches. They differ in practicality as well as interpretation. The so-called KaFit software framework implements several corresponding tools tailored to the KATRIN experiment. It is interfaced to SSC (section ??). A description of KaFit can e.g. be found in [Kle14]. This chapter outlines a selection of statistical approaches following mainly the statistics chapter of the Review of Particle Physics [Tan+18]. Additionally, within this thesis the implementations in KaFit were extended, which will also be described.

#### 3.1. The Maximum Likelihood Estimator

The likelihood is the probability of a measurement outcome given a hypothesis. A hypothesis depending on a parameter vector  $\boldsymbol{\theta}$  is called a composite hypothesis. A measurement outcome can be quantified by a vector of observed values  $\mathbf{x}$ . The probability  $P$  of  $\mathbf{x}$  given a hypothesis in dependence of  $\boldsymbol{\theta}$  is called the likelihood function

$$L(\boldsymbol{\theta}) = P(\mathbf{x} \mid \boldsymbol{\theta}). \quad (3.1)$$

If  $p$  denotes the probability for one observed value  $x_i$  in  $\mathbf{x}$ , then the likelihood function can be written as a product

$$L(\boldsymbol{\theta}) = \prod_i p(x_i \mid \boldsymbol{\theta}). \quad (3.2)$$

The parameter vector  $\hat{\boldsymbol{\theta}}$  that maximizes the likelihood function is called the maximum likelihood estimator (MLE) for the true values of  $\boldsymbol{\theta}$ .

#### 3.2. The KATRIN Likelihood

The MLE-method can be applied to a KATRIN measurement as follows: The data vector is given by a set of  $n$  electron counts  $\{N_{\text{obs},i}\}$  measured at different retarding potentials  $qU_i$ . The hypothesis is that these counts follow a Poisson distribution with predicted expected electron counts  $\{N_{\text{theo},i}\}$  as e.g. in (2.47). For sufficiently high counts the Poisson distribution can be approximated by a Gaussian distribution  $\mathcal{N}(x, \mu, \sigma)$  with mean  $\mu = N_{\text{theo},i}(\boldsymbol{\theta})$  and standard deviation  $\sigma = \sqrt{N_{\text{obs},i}}$ . The likelihood function then reads

$$L(\boldsymbol{\theta}) = \prod_i^n \mathcal{N}\left(N_{\text{obs},i}, \mu = N_{\text{theo},i}(\boldsymbol{\theta}), \sigma = \sqrt{N_{\text{obs},i}}\right). \quad (3.3)$$

Commonly, instead of maximizing the likelihood function, its negative logarithm is minimized and a factor 2 is introduced

$$-2 \ln L(\boldsymbol{\theta}) = \chi^2(\boldsymbol{\theta}) = \sum_i^n \left( \frac{N_{\text{obs},i} - N_{\text{theo},i}(\boldsymbol{\theta})}{\sqrt{N_{\text{obs},i}}} \right)^2 + \text{constants}. \quad (3.4)$$

Under the made assumptions this expression is a sum of  $n$  standard normal distributed random variables and hence, follows the Pearson's chi-square statistic with  $n - \dim\boldsymbol{\theta}$  degrees of freedom. Its minimization yields the MLE estimator  $\hat{\boldsymbol{\theta}}$  for  $\boldsymbol{\theta}$ . Accordingly, the value  $\chi^2(\hat{\boldsymbol{\theta}})$  is a measure for the goodness-of-fit.

The parameter of interest in  $\boldsymbol{\theta}$  is the neutrino mass squared  $m_\nu^2$ . Furthermore,  $\boldsymbol{\theta}$  typically comprises the endpoint of the tritium  $\beta$  spectrum  $E_0$  (2.11), an overall normalization factor for the counts  $A_S$  and the rate of the background counts  $R_{bg}$ . For the later two see (2.47).

### 3.3. Confidence and Credible Intervals

The presented maximum likelihood method provides point estimates  $\hat{\boldsymbol{\theta}}$ . However, additional information can be provided by interval estimates. There are two main approaches to statistical inference, which may be called Bayesian and frequentist. They differ in their interpretation of probability which becomes especially evident by the interval estimates typically associated with the two approaches.

#### 3.3.1. Bayesian Credible Intervals

The likelihood  $L(\mathbf{x} | \boldsymbol{\theta})$  is a probability distribution of the data  $\mathbf{x}$  given the parameters  $\boldsymbol{\theta}$ . Using Bayes theorem the likelihood can be transformed into a probability density for the parameters  $\boldsymbol{\theta}$  by multiplication with a prior distribution  $\pi(\boldsymbol{\theta})$  and normalization to 1

$$P(\boldsymbol{\theta} | \mathbf{x}) = \frac{L(\mathbf{x} | \boldsymbol{\theta})\pi(\boldsymbol{\theta})}{\int L(\mathbf{x} | \boldsymbol{\theta}')\pi(\boldsymbol{\theta}') d\boldsymbol{\theta}'} . \quad (3.5)$$

Here,  $P(\boldsymbol{\theta} | \mathbf{x})$  is the so-called posterior distribution. So-called credible regions, in which the true parameters lie with a certain probability  $\alpha$ , can be extracted. Typical values for  $\alpha$  are 68 % and 95 %. When  $\boldsymbol{\theta}$  is one dimensional a credible region becomes a credible interval.

#### 3.3.2. Frequentist Confidence Intervals

In frequentist statistics, probability is interpreted as the frequency of the outcome of a repeatable experiment. A confidence region  $C(\alpha)$  of confidence level (CL)  $\alpha$  for a parameter vector with true value  $\boldsymbol{\theta}_T$  is the following: If an experiment were to be repeated many times and the confidence region  $C(\alpha)$  were to be constructed each time according to the same recipe, it would contain the true parameter  $\boldsymbol{\theta}_T$  a fraction of at least  $\alpha$  times. Typical values for  $\alpha$  are chosen as quantiles of the Gaussian distribution in steps of standard deviations  $\sigma$ . E.g. the 1- and 2- $\sigma$  levels are 68 % and 95 %. The Neyman construction [Neyman1937] or its extension, the unified approach by Feldman and Cousins [Feldman1998], yield such confidence regions. When  $\boldsymbol{\theta}$  is one dimensional a confidence region becomes a confidence interval.

Approximated confidence regions can be extracted from the likelihood. If the likelihood follows the form of a multivariate Gaussian distribution in  $\boldsymbol{\theta}$ , then the hyper surface defined by

$$\ln L(\boldsymbol{\theta}) = \ln L(\hat{\boldsymbol{\theta}}) - \frac{s^2}{2} \quad (3.6)$$

encloses a  $s$ - $\sigma$  confidence region for  $\boldsymbol{\theta}$ . This is the case for the KATRIN chi-square likelihood.

### 3.4. Nuisance Parameters and the Profile Likelihood Method

### 3.5. The KaFit and SSC Software Frameworks

### 3.6. KATRIN's Sensitivity to the Electron Antineutrino Mass

## 4. The Energy-Dependence of Inelastic Electron Scattering within the KATRIN Source Section

**[Clean up!]** A  $\beta$  electron's probability to scatter when traveling through the STS depends on the scattering cross section  $\sigma$  (2.19). The cross section  $\sigma$  in turn depends on the kinetic energy  $E_{\text{kin}}$  of the electron:  $\sigma \equiv \sigma(E_{\text{kin}})$ . This dependence has been neglected in the modeling of the electron counts in section 2.2.5.

**To Do**

### 4.1. Cross Section of Tritium- $\beta$ Electrons Scattering from Hydrogen Isotopologues

In a KATRIN measurement there exists a minimum retarding energy  $qU_{\min}$  and only electrons with a kinetic energy greater than  $qU_{\min}$  can reach the detector. A scattering cross section averaged over the kinetic energy of the electrons reaching the detector was assumed

$$\sigma = \sigma_{\text{avg}} = \frac{1}{\Delta E_{\text{kin}}} \int_{qU_{\min}}^{qU_{\min} + \Delta E_{\text{kin}}} \sigma(E_{\text{kin}}) dE_{\text{kin}} \quad \text{with} \quad \Delta E_{\text{kin}} = E_0^{\text{eff}} - qU_{\min}. \quad (4.1)$$

Here, the “effective endpoint”  $E_0^{\text{eff}}$  denotes the highest kinetic energy of  $\beta$  electrons reaching the detector. It does not necessarily match the endpoint of the tritium  $\beta$  spectrum as experiment specific effects might shift it.  $E_0^{\text{eff}} = 18.575 \text{ eV}$  is assumed. Instead of an average cross section an energy dependent formula can be used. Incorporating the energy dependence makes the model more complicated and slower to compute; neglecting it may lead to wrong results. More light will be shed on both aspects within this chapter.

The total scattering cross section is a sum of the cross section for elastic and inelastic scattering.

$$\sigma(E_{\text{kin}}) = \sigma_{\text{el}} + \sigma_{\text{inel}}(E_{\text{kin}}). \quad (4.2)$$

Only the energy dependence of the inelastic scattering cross section will be considered. This is justified for now as according to [Ang+05] the cross section for elastic scattering is about an order of magnitude smaller than the one for inelastic scattering. An expression for the inelastic cross section for electrons scattering from hydrogen molecules can be found in [Liu73]. Two expressions are given, one for relativistic incident particles and one for non-relativistic incident particles. For the maximum relativistic  $\beta$  factor of  $\beta$  electrons from tritium decay one finds

$$\begin{aligned} \beta(E_{\text{kin}}, m) &= \sqrt{1 - \frac{1}{(\frac{E_{\text{kin}}}{m} + 1)^2}} \\ \beta_{\max} &= \beta(E_0^{\text{eff}}) \approx 18.6 \text{ keV}, m_e \approx 511 \text{ keV} \approx 0.26 \end{aligned} \quad (4.3)$$

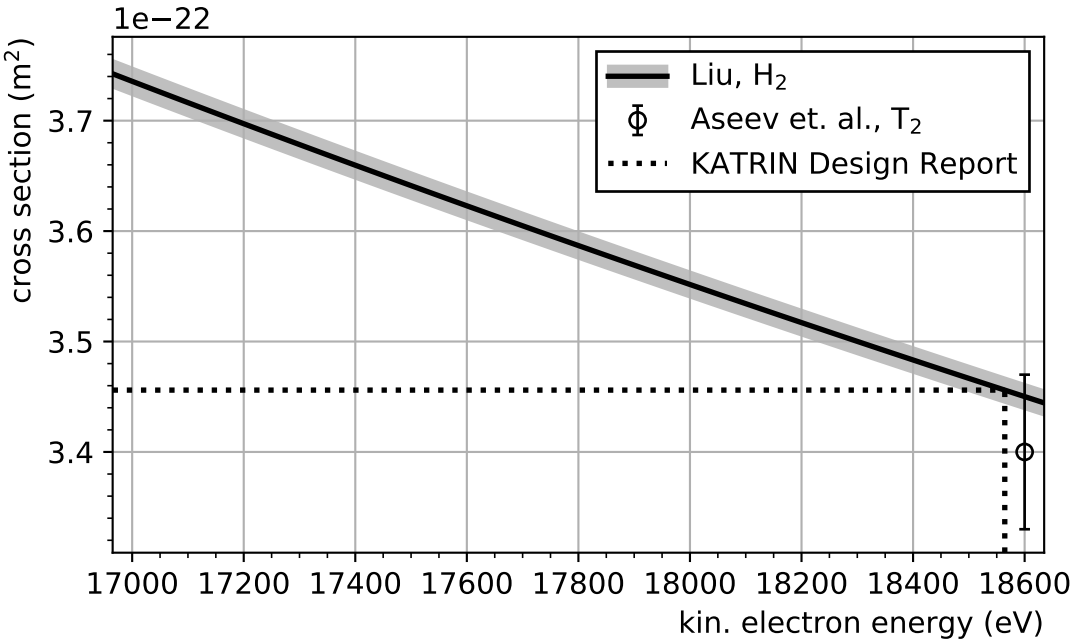


**Figure 4.1.: Inelastic cross section for non-relativistic electrons scattering from molecular hydrogen isotopologues.** Shown is the theoretical calculation by Liu along with its uncertainty [Liu73], the measurement by Aseev et. al. at the Troitsk experiment [AB+00] and the value stated in the KATRIN design report [Ang+05]. (The values are also listed in table 4.1.) The depicted energy interval matches the measurement interval of the First Tritium (FT) campaign. **FIX et al.**

Traveling at approximately a forth of the speed of light, the  $\beta$  electrons are assumed to be non-relativistic. Then, the given expression for the energy dependent cross section is

$$\sigma(E_{\text{kin}}) = (4\pi a_0^2) \cdot \left( \frac{E_{\text{kin}}}{R} \right)^{-1} \cdot \left[ C_1 \cdot \ln \left( \frac{E_{\text{kin}}}{R} \right) + C_2 \right] \quad (4.4)$$

with the Bohr radius  $a_0$ , the Rydberg energy  $R$  and two constants given as

$$C_1 = 1.5487 \quad \text{and} \quad C_2 = 2.2212 \pm 0.0434. \quad (4.5)$$

Note that in other works  $C_2 = 2.4036$  [Liu87] and  $C_2 = 1.53$  [Ger75] are given. The value in (4.5) from [Liu73] was chosen to enable comparability with the KATRIN Design Report [Ang+05].

Furthermore, the total inelastic scattering cross section was measured at the Troitsk experiment and the KATRIN Design Report states a reference value. The values are listed in table 4.1. The reference value matches the theoretical calculation using (4.4) at a kinetic energy of  $E_{\text{kin}} \approx 18564.4$  eV which would be the center of a  $\Delta E_{\text{kin}} = 20$  eV KATRIN measurement interval. Note that in the KATRIN reference measurement interval  $[E_0^{\text{eff}} - 30 \text{ eV}, E_0^{\text{eff}}]$  the cross section varies  $\sim 0.14\%$ . This variation is below its theoretical uncertainty given by (4.5). In the measurement interval of the FT campaign it varies  $\sim 8\%$ .

## 4.2. Motivation and Significance for the KATRIN Experiment

The motivation to implement an energy dependent cross section into the SSC framework is two-fold:

**Table 4.1.: Energy-dependence of the inelastic scattering cross section.** Listed are important values with reference to KATRIN. Except for the measured value, they are obtained using (4.4). The values are given relative to an assumed endpoint of the measured spectrum  $E_0^{\text{eff}} = 18\,575 \text{ eV}$ .

kin. energy	cross section ( $10^{-22} \text{ m}$ )	Note
$E_0^{\text{eff}} - 1600 \text{ eV}$	3.740	largest range in FT campaign
$E_0^{\text{eff}} - 90 \text{ eV}$	3.469	largest range in KNM1 campaign
$E_0^{\text{eff}} - 30 \text{ eV}$	3.459	KATRIN reference measurement interval [Ang+05]
$E_0^{\text{eff}} - 10 \text{ eV}$	3.456	KATRIN reference value [Ang+05]
$E_0^{\text{eff}}$	3.454	endpoint of tritium $\beta$ spectrum
18 600 eV	$3.40 \pm 0.07$	measured at the Troitsk experiment [AB+00]

**Deep scans:** According to [Gro15] for a neutrino mass determination with the precision goals of KATRIN, the inelastic scattering cross section has to be known with an upper uncertainty of  $0.0055 \times 10^{-22} \text{ m}$  (0.16 %). This requirement might be surpassed by neglecting that the scattering cross section is not constant, but varies with energy. According to table 4.1 the requirement is fulfilled in a measurement interval of  $[E_0^{\text{eff}} - 30 \text{ eV}, E_0^{\text{eff}}]$ . According to (4.4) it is violated if the lower bound of the measurement interval is below 18 531 eV. Scans deeper into the tritium  $\beta$  spectrum increase the count rates and hence, improve the statistic uncertainty on the neutrino mass. Also, for the search of sterile neutrinos deeper scans are necessary. On top of that, deeper scans have already been performed e.g. in the FT campaign and help to establish an even better understanding of the KATRIN apparatus. In these cases the energy dependence is not negligible.

**Comparability:** A possible cross-check for software is its comparison to other software that was developed independently. SSC is part of a data fitting suit. Other fitting software exists within the KATRIN collaboration that uses an energy dependent scattering cross section, e.g. FITRIUM [Kar+19]. Furthermore, SSC is commonly cross-checked against a Monte-Carlo particle tracking software called KASSIOPEIA [KAT19] which also implements an energy dependent scattering cross section.

## 4.3. An Energy-Dependent Scattering Model within the KATRIN Formalism

### 4.3.1. Model Description

**Table 4.2.: The scattering probabilities** averaged over all starting positions and starting angles in the WGTS. Both the values from a Monte Carlo (MC) simulation and the values according to (2.41) are given. The later ones can also be found in [Gro15; Kle14] and in the code of the SSC framework [KAT19].

scattering count	MC particle tracking [Gro15]	equation (2.41)
0	$0.415 \pm 0.002$	0.41334
1	$0.292 \pm 0.002$	0.29266
2	$0.166 \pm 0.001$	0.16733
3	$0.079 \pm 0.001$	0.07913
4	$0.031 \pm 0.001$	0.03178

The energy-dependence of the scattering cross section enters into the calculation of the scattering probabilities (2.24). In the derivation the dependence on the starting energy  $E_S$  was neglected. Instead an average starting energy and hence, an average scattering cross

section  $\sigma(18\,564.4\,\text{eV}) = 3.456 \times 10^{-22}\,\text{m}^2$  was assumed. For this case table 4.2 lists the scattering probabilities averaged over all starting positions and pitch angles in the WGTS. In the energy dependent case the scattering cross section has to be adapted to the starting energy of the  $\beta$  electrons. In other words, the scattering probabilities follow a Poisson distribution averaged over starting positions and pitch angles of  $\beta$  electrons. Analogously to the derivation in section 2.2.5 they read:

$$\mu(E_S, z_S, \theta_S) = \frac{\sigma(E_S)}{\cos \theta_S} \int_{z_S}^{L/2} \rho(z) dz \quad (4.6a)$$

$$P_l(E_S, z_S, \theta_S) = \text{Poisson}(\mu(E_S, z_S, \theta_S), l) \quad (4.6b)$$

$$\bar{P}_l(E_S) = \frac{1}{L \cdot (1 - \cos(\theta_{\max}))} \int_{-L/2}^{L/2} \int_0^{\theta_{\max}} \sin(\theta_S) \text{Poisson}(\mu(E_S, z_S, \theta_S), l) d\theta_S dz_S. \quad (4.6c)$$

Here,  $\bar{P}_l(E_S)$  in the final equation (4.6c) denotes the probability of  $l$ -fold scattering for a  $\beta$  electron with a starting energy  $E_S$  averaged over all starting positions and pitch angles. This model will be denoted Poisson model. It is expected to be accurate for the probability of no scattering  $\bar{P}_0(E_S)$ .

But, depending on the required accuracy, for 1 or more scatterings this Poisson model does not necessarily hold. A scattering electron loses energy. Due to a lower energy the scattering cross section increases and the electron becomes more likely to scatter again. In other words, the probability of individual scattering processes are no longer independent. This violates one of the preconditions to model the scattering probabilities via a Poisson distribution. Another model is suggested. It assumes a constant gas density  $\rho$ , a fixed energy loss of  $\epsilon$  per scattering and a source length of  $L$ :

$$\mu(E, \theta_S) = \frac{\sigma(E)\rho L}{\cos \theta_S} \quad (4.7a)$$

$$p_0(E, \theta_S, n) = \left(1 - \frac{\mu(E, \theta_S)}{N}\right)^n \quad (4.7b)$$

$$p_l(E, \theta_S, n) = \sum_{k=l}^n p_{l-1}(E, \theta_S, k-1) (1 - p_0(E - (l-1)\epsilon, \theta_S, 1)) p_0(E - l\epsilon, \theta_S, n-k) \quad (4.7c)$$

$$\bar{p}_l(E, \theta_S) = \frac{1}{L} \int_0^L p_l(E, \theta_S, \left\lceil N \frac{z_S}{L} \right\rceil) dz_S \quad (4.7d)$$

$$P_l^*(E_S, \theta_S) = \lim_{N \rightarrow \infty} \bar{p}_l(E_S, \theta_S) \quad (4.7e)$$

$$\bar{P}_l^*(E_S) = \frac{1}{1 - \cos \theta_{\max}} \int_0^{\theta_{\max}} P_l^*(E_S, \theta_S) d\theta_S. \quad (4.7f)$$

Here,  $\bar{P}_l^*(E_S)$  in the final equation (4.7f) denotes the probability of  $l$ -fold scattering for a  $\beta$  electron with a starting energy  $E_S$  averaged over all starting positions and pitch angles assuming a fixed energy loss  $\epsilon$  per scattering. This model will be denoted extended model. A descriptive derivation is given in appendix A.1.

The extended model is evaluated numerically as it includes one limit and two integrals. A balance between the numerical accuracy and the evaluation run time had to be found. Details can be found in the appendix A.2. The probability for 1-fold scattering could be calculated with an accuracy on the  $10^{-5}$  level and for 2-fold scattering with an accuracy on the  $10^{-3}$  level.

The suggested extended model is only valid for a fixed energy loss per scattering  $\epsilon$ . The value  $\epsilon = 14.1\,\text{eV}$  was chosen as it is the most probable energy loss for electrons travelling

through tritium gas according to [AB+00]. A more accurate description would use the energy loss probability density. This has not yet been considered.

Figure 4.2 shows the Poisson model along with the suggested extended model. The results are discussed in the following paragraphs.

### 4.3.2. Model Discussion

#### Model compatibility

For 1-fold scattering the difference between the Poisson and the extended model is on the  $10^{-4}$  level. For 2-fold scattering the accuracy of the numerical evaluation of the extended model is not yet sufficient to distinguish it from the Poisson model. Table 4.2 lists the scattering probabilities for an energy independent Poisson model and a reference cross section  $\sigma(18\,564.4\,\text{eV}) = 3.456 \times 10^{-22}\,\text{m}$  given in the KATRIN Design Report [Ang+05]. It also lists the outcome of a Monte Carlo simulation taken from [Gro15]. As expected the energy dependent Poisson model recovers the energy independent model exactly at the corresponding energy of 18 564.4 eV. Furthermore, within the endpoint region of the tritium  $\beta$  spectrum all models match the Monte Carlo simulation within its uncertainty.

#### Trend of energy-dependence

For a decreasing starting energy of  $\beta$  electrons the probability for no and 1-fold scattering also decreases while the probability for 2-fold scattering increases. This is expected for the following reasons. For a starting energy of  $E_S = 18\,564.4\,\text{eV}$  the expected amount of scatterings  $\mu$  (4.6a) averaged over all starting positions  $z_S$  and pitch angles  $\theta_S$  is

$$\bar{\mu} = \frac{1}{L \cdot (1 - \cos(\theta_{\max}))} \int_{-L/2}^{L/2} \int_0^{\theta_{\max}} \sin(\theta_S) \mu(E_S, z_S, \theta_S) d\theta_S dz_S = 1.077. \quad (4.8)$$

In other words,  $\beta$  electrons with a starting energy near the endpoint of the tritium  $\beta$  spectrum are expected to scatter around  $\bar{\mu} = 1.077$  times when travelling through the WGTS. If the starting energy decreases and hence, scattering becomes more likely it becomes more likely to scatter more than  $\bar{\mu}$  times and less likely to scatter less than  $\bar{\mu}$  times. Thus, the probability for no and 1-fold scattering decreases along with the starting energy of the  $\beta$  electrons. At the same time the probability for more than 1 scatterings increases for lower starting energies. This intuitive reasoning is also reflected by deriving the scattering probabilities (4.6b) for the starting energy where  $\mu$  denotes the expected scattering count (4.6a)

$$\frac{dP_l(E_S, z_S, \theta_S)}{dE_S} = \underbrace{\text{Poisson}(\mu(E_S, z_S, \theta_S), l)}_{\geq 0} \cdot \underbrace{\left( \frac{l}{\mu(E_S, z_S, \theta_S)} - 1 \right)}_{(*)} \cdot \underbrace{\frac{\int_{z_S}^L \rho(z) dz}{L \cos \theta_S}}_{>0} \cdot \underbrace{\frac{d\sigma(E_S)}{dE_S}}_{<0}. \quad (4.9)$$

The sign of the derivative is determined by the sign of  $(*)$  which follows approximately the above reasoning being negative for  $l < \bar{\mu}$  and positive for  $l > \bar{\mu}$ .

## 4.4. Implementation of the Energy-Dependent Scattering Model

### 4.4.1. Description of the Implementation

### 4.4.2. Performance and Accuracy Considerations

The suggested extended model (4.7) at its current stage is computationally too expensive to be used in a fitting procedure. Note that a similar model has been derived for a fixed

change of the pitch angle  $\theta$  per scattering in [Gro15]. This model for angular changes is implemented in the SSC software and can be used in fitting procedures. Though, an important difference is that the determination of the count rate requires an integral over the starting energy  $E_S$  in (2.14). Hence, the energy dependent scattering probabilities have to be recomputed in every step of the numerical integration. This is not the case for the model considering the angular changes.

Albeit the energy dependent Poisson model might not fully hold in the case of an energy dependent cross section, figure 4.2 shows that for larger measurement intervals it is more accurate than assuming energy independent scattering probabilities. Hence, it is a reasonable choice to implement the energy dependent Poisson model into the SSC software. This was done. As mentioned the energy dependent scattering probabilities have to be recomputed in every step of the numerical integration in (2.14) over the  $\beta$  electron energy. The impact on the run time was probed for 5 different MTDs. They differ in the amount and range of retarding potentials. Both aspects should influence the run time. The run time should be approximately linear in the amount of retarding potentials. The run time should get longer the wider the range of the retarding potentials is as the numerically evaluated integral over energies in (2.14) then stretches over a wider range. Figure 4.3 shows that the run times increase by a factor of approximately 40 – 120 between assuming a constant cross section and an energy dependent one.

## 4.5. Effect on the Inferred Neutrino Mass

### 4.5.1. Neutrino Mass Shift within a Standard KATRIN Measurement Interval

#### ToDo

**[Numbers can not be reconciled with shifting the cross section. What to do about it?]** In order to determine the influence of the energy dependence of the scattering cross section on the neutrino mass determination the so-called “shift method” was used. A description can e.g. be found in [Sei19].

#### ToDo

**[Write own description]** In short, an integrated rate using the energy dependent Poisson model for the scattering probabilities was simulated and fitted to a model using the constant Poisson model. One obtains a deviation of the fitted and simulated neutrino mass, the neutrino mass shift. The procedure was repeated for multiple measurement intervals using the settings from the KATRIN Design Report [Ang+05] for a 3-year measurement. A comparison of the statistical uncertainty on the neutrino mass and its shift is shown in figure 4.4 depending on the measurement interval. For a measurement interval of approximately 35 eV the shift and the statistical uncertainty are approximately equal

$$\sigma(m_\nu) \approx \sqrt{0.015} \text{eV} = 122 \text{ meV (68 \% C.L.)} . \quad (4.10)$$

### 4.5.2. Neutrino Mass Shift in an Extended Measurement Interval

In spring 2019 the so-called KNM1 campaign started. The measurement interval was 90 eV. The MTD had been optimized according to the up-to-date status of the KATRIN experiment which did not match the KATRIN Design Report in all aspects. The study on the neutrino mass shift was redone scaling the MTD of the KNM1 campaign to 3 years and using the corresponding KNM1-settings. The neutrino mass shift then would be 297 meV.

## 4.6. Conclusion and Outlook

The energy dependence of the scattering cross section enters into the calculation of the scattering probabilities. An accurate modelling of the energy dependent scattering probabilities is challenging due to performance reasons, but modelling them according to a

Poisson distribution is possible. It was shown that the difference between the Poisson model and a more accurate model for 1-fold scattering is on the  $10^{-4}$  level. The cases for more than 1 scatterings need further investigation. Also a fixed energy loss per scattering was assumed instead of a energy loss probability distribution. Future work might consider these aspects and what influence a more accurate modeling on the scattering probabilities has on the neutrino mass determination.

Given the KATRIN uncertainty budget, when modeling the energy dependent scattering probabilities via a Poisson distribution, the energy dependence of the scattering cross section is not negligible for measurement intervals that extend more than 35 eV below the endpoint of the tritium  $\beta$  spectrum.

Including the energy dependence in the analysis increases the run time of the fitting procedure significantly. Future work might consider to precalculate the scattering probabilities for different fixed energies and use interpolation techniques for energies in-between the fixed ones.

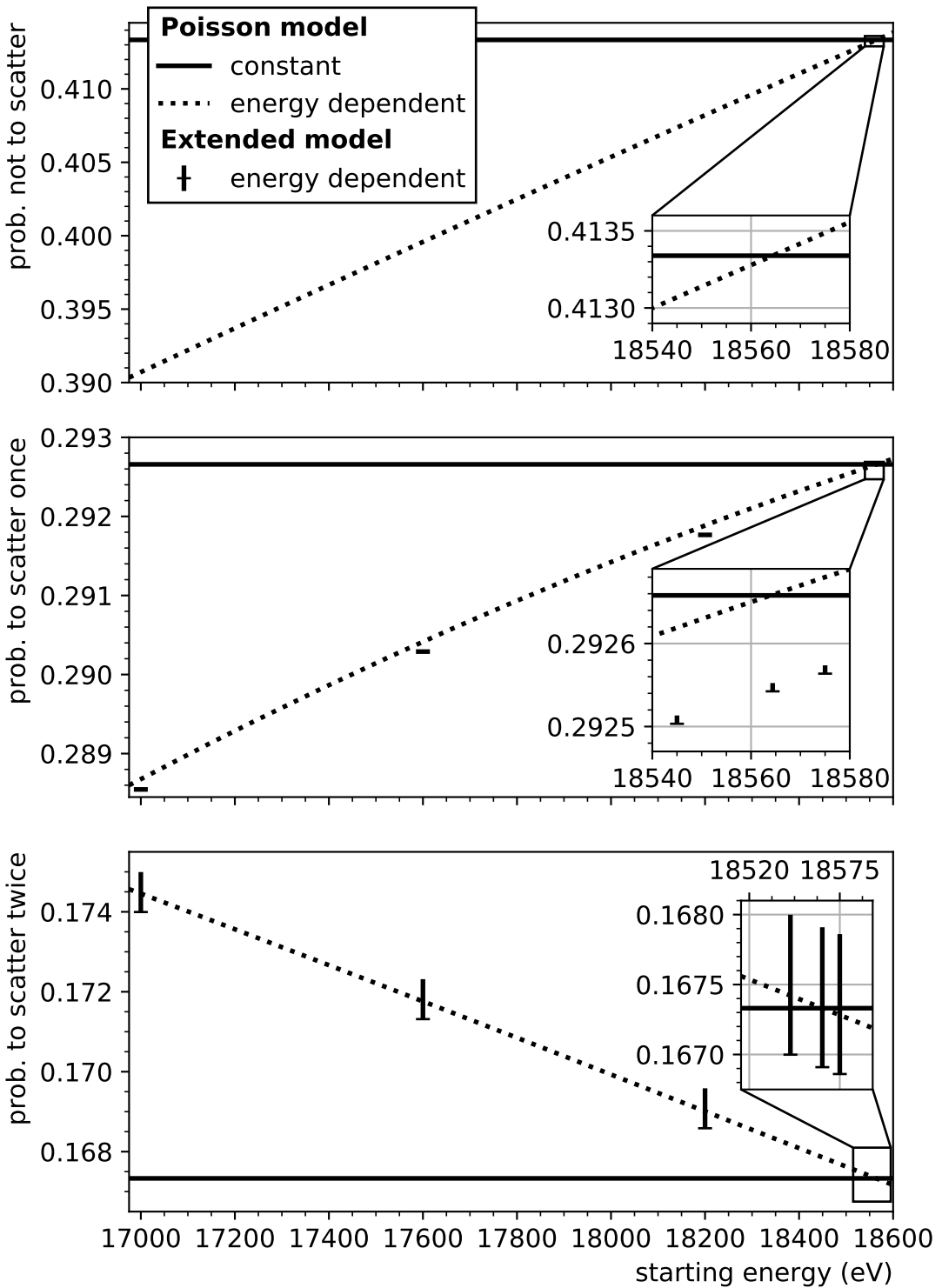


**Figure 4.2.: Scattering probabilities.** Shown are from top to bottom the probability for no, 1-fold and 2-fold scattering averaged over all starting positions and starting pitch angles of  $\beta$  electrons. Depending on the required accuracy, for 1-fold and 2-fold scattering the Poisson model does not hold. The markers show an extended model as described in the text. Its numerical evaluation suffers from a one-sided uncertainty (of  $\sim 10^{-5}$  for 1-fold and  $\sim 10^{-3}$  for 2-fold scattering) depicted as uncertainty bars. The inset shows an energy span around the endpoint of the tritium  $\beta$  spectrum. The full energy range matches the measurement interval of the First Tritium (FT) campaign.

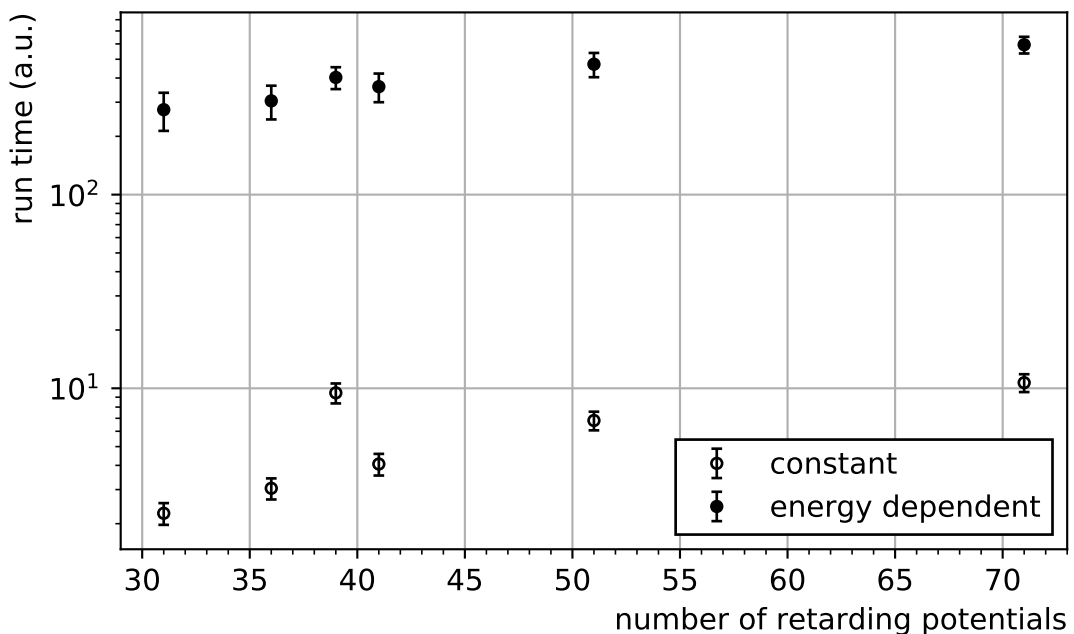


**Figure 4.3.: Run-time comparison between using an energy-dependent and independent cross section.** Shown are the run times for a fit of a simulated model to itself for different MTDs. The MTDs for the ranges 20, 25, 30, 40 and 50 eV are taken from the KATRIN design report [Ang+05] and have a rising number of retarding potentials. A further 90 eV-wide MTD of the KNM1 campaign was used. It contains 39 retarding potentials. The corresponding run time lies above the trend line as the width of the measurement interval is wider. For each MTD 30 fits were performed. The run times were clocked for a constant and an energy-dependent cross section.

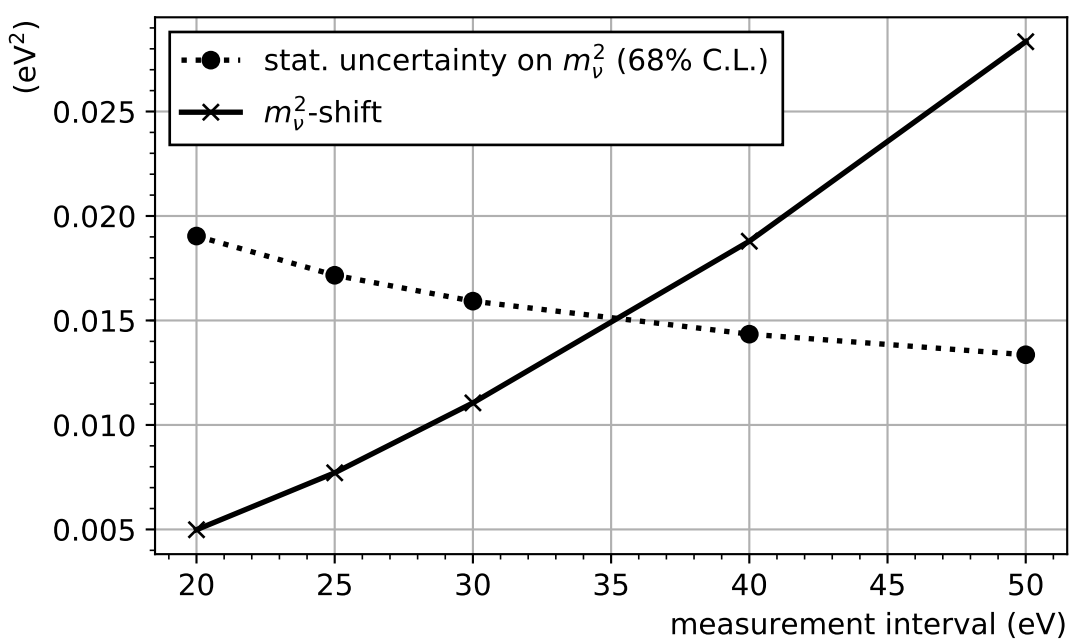


**Figure 4.4.: Neutrino mass shift due to an energy dependent inelastic scattering cross section** as calculated by SSC for 5 measurement intervals. The configuration for the calculation, especially the measurement time distribution (MTD), follows the KATRIN Design Report [Ang+05]. For comparison the statistical uncertainty is plotted as well. It is derived from the profile likelihood. The lines between the 5 markers are linear interpolations.

## 5. Parameter Inference Using an Energy Loss Model for Inelastically-Scattering Electrons Derived from KATRIN Data

### 5.1. The Preliminary KATRIN Energy Loss Model

### 5.2. Statistical Prerequisites

#### 5.2.1. Combination of Commissioning and Neutrino Mass Measurements

If two measurements share a set of parameters  $\boldsymbol{\theta}_s$ , but have additionally an individual set of parameters  $\boldsymbol{\theta}_1$  and  $\boldsymbol{\theta}_2$  and different sets of observations a combined likelihood is given by the product of the single likelihoods  $L_1$  and  $L_2$

$$-2 \ln L(\boldsymbol{\theta}_s, \boldsymbol{\theta}_1, \boldsymbol{\theta}_2) = -2 \ln L_1(\boldsymbol{\theta}_s, \boldsymbol{\theta}_1) - 2 \ln L_2(\boldsymbol{\theta}_s, \boldsymbol{\theta}_2). \quad (5.1)$$

In the case of KATRIN the first measurement could be sensitive to the neutrino mass whereas say the second measurement could have been a calibration using the electron gun and be sensitive to parameters of the response function (2.46). Combining both likelihoods would incorporate the uncertainties on the parameters of the response function in the neutrino mass determination. Currently, no software framework exists that allows the construction of combined likelihoods of KATRIN neutrino mass and calibration measurements. Instead the following approximation can be made. The calibration measurement is evaluated independently and one obtains estimates  $\hat{\boldsymbol{\theta}}_{s,2}$ , and an estimated covariance matrix  $\hat{V}_{s,2}$  for all components of  $\boldsymbol{\theta}_s$  that the calibration measurement is sensitive to. These can in turn be used to approximate the likelihood  $L_2$  at least in the dimension of  $\boldsymbol{\theta}_s$ . A choice that stands to reason for the approximation of  $L_2$  is a multivariate Gaussian distribution. For the purpose of parameter inference through minimization  $-2 \ln L_2$  needs only to be accurately approximated around its minimum. The choice of a multivariate Gaussian distribution corresponds a symmetric approximation of  $-\ln L_2$  around its minimum by a parabola. The KATRIN likelihood for a combination of a neutrino mass and a calibration measurement then reads

$$\begin{aligned} -2 \ln L(\boldsymbol{\theta}_s, \boldsymbol{\theta}_1, \boldsymbol{\theta}_2) &\approx -2 \ln L'(\boldsymbol{\theta}_s, \boldsymbol{\theta}_1) \\ &= \underbrace{\chi^2(\boldsymbol{\theta}_s, \boldsymbol{\theta}_1)}_{(1)} + \underbrace{(\boldsymbol{\theta}_s - \hat{\boldsymbol{\theta}}_{s,2})^\top \hat{V}_{s,2}^{-1} (\boldsymbol{\theta}_s - \hat{\boldsymbol{\theta}}_{s,2})}_{(2)} + \text{constants} \\ &= \chi^2(\boldsymbol{\theta}_s, \boldsymbol{\theta}_1) - 2 \ln \mathcal{N}(\boldsymbol{\theta}_s, \hat{\boldsymbol{\theta}}_{s,2}, \hat{V}_{s,2}^{-1}) + \text{constants} \end{aligned} \quad (5.2)$$

Here, (1) is the chi-square expression (3.4) where the  $\boldsymbol{\theta}_s$  and  $\boldsymbol{\theta}_1$  can be written as one combined parameter vector  $\boldsymbol{\theta}$  for a neutrino mass measurement. And (2) resembles the negative log likelihood of the calibration measurement approximated by a multivariate Gaussian distribution. Terms having a form like (2) are also sometimes called “pull terms”

or ‘‘likelihood penalties’’. In the minimization process they ‘‘pull’’ the parameters  $\boldsymbol{\theta}_s$  towards  $\hat{\boldsymbol{\theta}}_{s,2}$  respectively ‘‘penalize’’/increase the negative log likelihood if  $\boldsymbol{\theta}_s$  and  $\hat{\boldsymbol{\theta}}_{s,2}$  differ.

The chi-square term (1) is a sum of  $n$  standard normal distributed random variables. Hence, as discussed, a likelihood only composed of the chi-square term (1) offers a goodness-of-fit criteria via the Pearson chi-square statistic. Note that for the combined likelihood this criteria might not hold. Two special cases can be considered where the chi-square characteristics hold approximately: First, the neutrino mass measurement, term (1), is not sensitive to the shared parameters  $d\chi^2(\boldsymbol{\theta}_s, \boldsymbol{\theta}_1)/d\boldsymbol{\theta}_s \approx 0$ . Then the MLE for the shared parameters will match the MLE by the calibration measurement  $\hat{\boldsymbol{\theta}}_s = \hat{\boldsymbol{\theta}}_{s,2}$  and term (2) will be 0. The combined likelihood evaluated at the MLE  $-2 \ln L(\hat{\boldsymbol{\theta}}_s, \hat{\boldsymbol{\theta}}_1)$  then follows a chi-square distribution with  $n - \dim \boldsymbol{\theta}_1 - \dim \boldsymbol{\theta}_s$  degrees of freedom. Second, if the neutrino mass measurement is sensitive to some shared parameters  $d\chi^2(\boldsymbol{\theta}_s, \boldsymbol{\theta}_1)/d\boldsymbol{\theta}_s \neq 0$ , then one might argue, that term (2) evaluated at the MLE  $\hat{\boldsymbol{\theta}}_s \neq \hat{\boldsymbol{\theta}}_{s,2}$  is a sum of standard normal distributed random variables. If this holds, the combined likelihood evaluated at the MLE  $-2 \ln L(\hat{\boldsymbol{\theta}}_s, \hat{\boldsymbol{\theta}}_1)$  follows a chi-square distribution with  $n - \dim \boldsymbol{\theta}_1$  degrees of freedom.

For example, a standard KATRIN 3-year neutrino mass measurement is not at all sensitive to parameters of the energy loss function (2.34). Hence, adding a corresponding term (2) from a designated energy loss measurement will not influence the chi-square characteristics. However, a standard KATRIN neutrino mass measurement is even after a short measurement time sensitive to the gas column density (2.1). Adding a corresponding term (2) from (a naturally more sensitive) monitoring measurement would influence the

## ToDo

**[Add plots from ensemble test that proof statements.]**

### 5.2.2. Extension of the KaFit Software Framework

The likelihood  $L(\boldsymbol{\theta})$  can be multiplied by a function  $g(\boldsymbol{\theta})$

$$-2 \ln L'(\boldsymbol{\theta}) = -2 \ln L(\boldsymbol{\theta}) - 2 \ln g(\boldsymbol{\theta}). \quad (5.3)$$

This procedure may have different interpretations and usage scenarios. E.g. a comparison with (3.5) shows, if  $g$  is a prior probability distribution,  $L'$  becomes a non-normalized posterior distribution that can be used in a Bayesian analysis. A further interpretation is given in section 5.2.2.

KaFit allowed to choose  $g$  in 5.3 as a product of one-dimensional Gaussian distributions. Within this thesis the software was extended to allow products of other functions. Three function types were explicitly made available through a configuration file.

1. A reimplementation of a one-dimensional Gaussian distribution: The reimplementation was necessary to conveniently enable the combination of function types.
2. A multivariate Gaussian distribution: This enables the treatment of uncertainties quantified by calibration or monitor measurements as described in section 5.2.2. It can also be used as a prior distribution in a Bayesian analysis. Particularly, correlations can be respected.
3. A one-dimensional probability density, that is constant in the square root of a parameter, if it is positive and 0 otherwise:

$$g(\theta) = \begin{cases} 0 & \text{if } \theta \leq 0 \\ \text{constant} \cdot \frac{1}{\sqrt{\theta}} & \text{if } \theta > 0 \end{cases}. \quad (5.4)$$

This can be used as a uniform prior on the neutrino mass ( $\theta = m_\nu^2$ ). Formerly, it was only possible to use a uniform prior on the squared neutrino mass. A derivation of the form of  $g$  can be found in appendix B.

**ToDo**

An example on how to configure KaFit using the new feature is given in appendix [\[Add appendix\]](#).

### 5.3. A Sensitivity Study using the Recent Preliminary KATRIN Energy Loss Model

#### 5.4. Conclusion and Outlook



## **6. Conclusions and Outlook**



# Appendix

## A. Energy-Dependence of the Scattering Probabilities

[Better subcaption, introduction]

**ToDo**

### A.1. Modeling

A model for energy dependent scattering probabilities is derived. The expected amount of scatterings for a  $\beta$  electron when traveling through the whole WGTS volume of length  $L$  filled with a gas of constant density  $\rho$  is

$$\mu(E, \theta_S) = \frac{\sigma(E)\rho L}{\cos \theta_S}, \quad (\text{A.1})$$

where  $E$  denotes the electron's kinetic energy;  $\theta_S$  the starting pitch angle; and  $\sigma(E)$  the energy dependent scattering cross section.

The volume of the WGTS is divided into  $N$  slices of equal width  $w = L/N$ .  $N$  is chosen sufficiently large that the probability for a  $\beta$  electron to scatter twice within one slice is essentially zero. Then, for large  $N$  the probability to scatter within one slice is  $\mu(E, \theta_S)/N$ . The probability not to scatter within  $n < N$  slices is

$$p_0(E, \theta_S, n) = \left(1 - \frac{\mu(E, \theta_S)}{N}\right)^n. \quad (\text{A.2})$$

Using the well known limit for the Euler constant, one obtains for  $n = N$  and  $N \rightarrow \infty$  that  $p_0$  is a Poisson distribution with expectation  $\mu$  evaluated at 0

$$\lim_{N \rightarrow \infty} p_0(E, \theta_S, N) = \lim_{N \rightarrow \infty} \left(1 - \frac{\mu(E, \theta_S)}{N}\right)^N = e^{-\mu(E, \theta_S)}. \quad (\text{A.3})$$

Assuming a constant energy loss per scattering of  $\epsilon$  the probability to scatter  $l$  times within  $n < N$  slices can be expressed recursively

$$p_l(E, \theta_S, n) = \underbrace{\sum_{k=l}^n}_{(4)} \underbrace{p_{l-1}(E, \theta_S, k-1)}_{(1)} \underbrace{(1 - p_0(E - (l-1)\epsilon, \theta_S, 1))}_{(2)} \underbrace{p_0(E - l\epsilon, \theta_S, n-k)}_{(3)}. \quad (\text{A.4})$$

The terms have the following meaning:

- (1) Probability to scatter  $l-1$  times within  $k-1$  slices with a kinetic energy of  $E$ .
- (2) Probability to scatter once within the  $k$ th slice with a kinetic energy of  $E - (l-1)\epsilon$ .
- (3) Probability not to scatter within the remaining  $N-k$  slices.
- (4) Sum over all slices  $k$ . The sum starts at  $l$  because the probability to scatter  $l-1$  times within less than  $k = l-1$  slices (term (1)) is 0.

The probability to scatter  $l$  times can be averaged over all starting positions. The averaging sum can be further approximated by an integral as this helps cutting down on run time in a numerical evaluation

$$\bar{p}_l(E, \theta_S) = \frac{1}{N} \sum_{n_S=1}^N p_l(E, \theta_S, n_S) \approx \frac{1}{L} \int_0^L p_l(E, \theta_S, \left\lceil N \frac{z_S}{L} \right\rceil) dz_S. \quad (\text{A.5})$$

Then the limit  $N \rightarrow \infty$  is applied

$$P_l^*(E_S, \theta_S) = \lim_{N \rightarrow \infty} \bar{p}_l(E_S, \theta_S) \quad (\text{A.6})$$

$P_l^*(E_S, \theta_S)$  denotes the probability for a  $\beta$  electron to scatter  $l$  times when traveling through the whole WGTS with a starting energy  $E_S$  and pitch angle  $\theta_S$  averaged over all starting positions. Finally, this expression has to be averaged over all starting pitch angles in order to obtain the energy dependent scattering probabilities

$$\bar{P}_l^*(E_S) = \frac{1}{1 - \cos \theta_{\max}} \int_0^{\theta_{\max}} \sin \theta_S P_l^*(E_S, \theta_S) d\theta_S. \quad (\text{A.7})$$

## A.2. Numerical Evaluation

The energy dependent probability to scatter once  $\bar{P}_1^*$  in (A.7) was evaluated numerically. In (A.6) taking the limit  $N \rightarrow \infty$  was replaced by choosing a large  $N$ . The averaging integral over the starting positions (A.5) and pitch angles (A.7) was computed using Gaussian quadrature.

Figure A.1 shows the result in dependence of  $N$  and the order of the Gaussian quadrature. Both should be chosen as low as possible to cut down on run time but sufficiently high for the required accuracy. As a cross check, for an energy loss of  $\epsilon = 0$  eV per scattering, the suggested extended model (A.7) must recover the Poisson model (see (4.6)). For  $N = 10^6$  and using Gaussian quadrature of order 5, they differ approximately  $3 \times 10^{-6}$ . Furthermore, the numerical calculation converges from below, which can be interpreted as a one-sided numerical inaccuracy. The calculations for  $\epsilon = 14.1$  eV are shown in the lower row of figure A.1. They also show convergence on the  $10^{-5}$  level. Conclusively, the results make it plausible to assume a one-sided numerical inaccuracy on the  $10^{-5}$  level for  $N = 10^5$  and using Gaussian quadrature of order 5 for the integrals.

The corresponding run time to compute  $\bar{P}_1^*$  is in  $\mathcal{O}(N)$  as it requires a sum over all  $N$  slices. Note that the extended model is defined recursively and therefore, the run time for  $l$ -fold scattering is in  $\mathcal{O}(N^l)$ . Hence, computing the probability for 2-fold scattering would take 500000 times as long as for 1-fold scattering for the same  $10^{-5}$  accuracy. This was found not to be feasible. For 2-fold scattering  $N = 5000$  and also Gaussian quadrature of order 5 was chosen for a numerical accuracy on the  $10^{-3}$  level.

## B. Neutrino Mass Prior

A KATRIN analysis derives the squared neutrino mass  $m_\nu^2$ . Hence, in a Bayesian analysis a prior on  $m_\nu^2$  is required. A uniform prior on the neutrino mass  $m_\nu$  is a possible choice. The following lines derive a prior on  $m_\nu^2$  that resemble a uniform prior on  $m_\nu$ . Let  $f(m_\nu) = C = \text{constant}$  be the prior on  $m_\nu$  and  $g(m_\nu^2)$  be the prior on  $m_\nu^2$ . Starting from conservation of probability one derives

$$\begin{aligned} f(m_\nu) dm_\nu &= g(m_\nu^2) dm_\nu^2 \\ \Rightarrow g(m_\nu^2) &= f(m_\nu) \left( \frac{dm_\nu^2}{dm_\nu} \right)^{-1} \\ \Rightarrow g(m_\nu^2) &= C \frac{1}{2\sqrt{m_\nu^2}}. \end{aligned}$$

## C. Likelihood Extensions

Within this thesis the implementation of the likelihood in the KaFit framework was extended as described in section 5.2.2. It is possible to multiply the likelihood by different function types. Example excerpts from KaFit-XML-configurations are given below. **[Double]** is used as a placeholder for a number; and **[Index\*]** for a parameter index. E.g. the neutrino mass squared has the parameter index 0. A new **Penalty**-tag was introduced as sub-tag of the **LoglikelihoodKatrin**-tag:

```
<LoglikelihoodKatrin
    Name="myKatrinLogL" PDF="Gauss" RunSource="myRunGen"
    SpectrumSimulator="mySpecSim">
    <Penalty>
        <!-- Penalty Type -->
    </Penalty>
</LoglikelihoodKatrin>
```

`<!-- Penalty Type -->` can be substituted by one or more of the following tags:

### Multivariate Gaussian Distribution

The attribute **Mean** specifies the mean of a parameter; **Std** the standard deviation; and one or more **Correlation**-sub-tags the correlations between the parameters specified by the **Parameter**-tags.

```
<MultivarNorm>
    <Parameter Index="[Index1]" Mean="[Double]" Std="[Double]" />
    <Parameter Index="[Index2]" Mean="[Double]" Std="[Double]" />
    <!-- ... -->
    <Correlation Index1="[Index1]" Index2="[Index2]" Value="[Double]" />
    <!-- ... -->
</MultivarNorm>
```

### One-Dimensional Gaussian Distribution

Analogously to the multivariate, a one-dimensional Gaussian distribution can be used:

```
<Gaussian ParamIndex="[Index]" Mean="[Double]" Std="[Double]" />
```

### Uniform Neutrino Mass Prior

A constant prior on the neutrino can be set via the following tag:

```
<ConstInSqrt ParamIndex="0" />
```

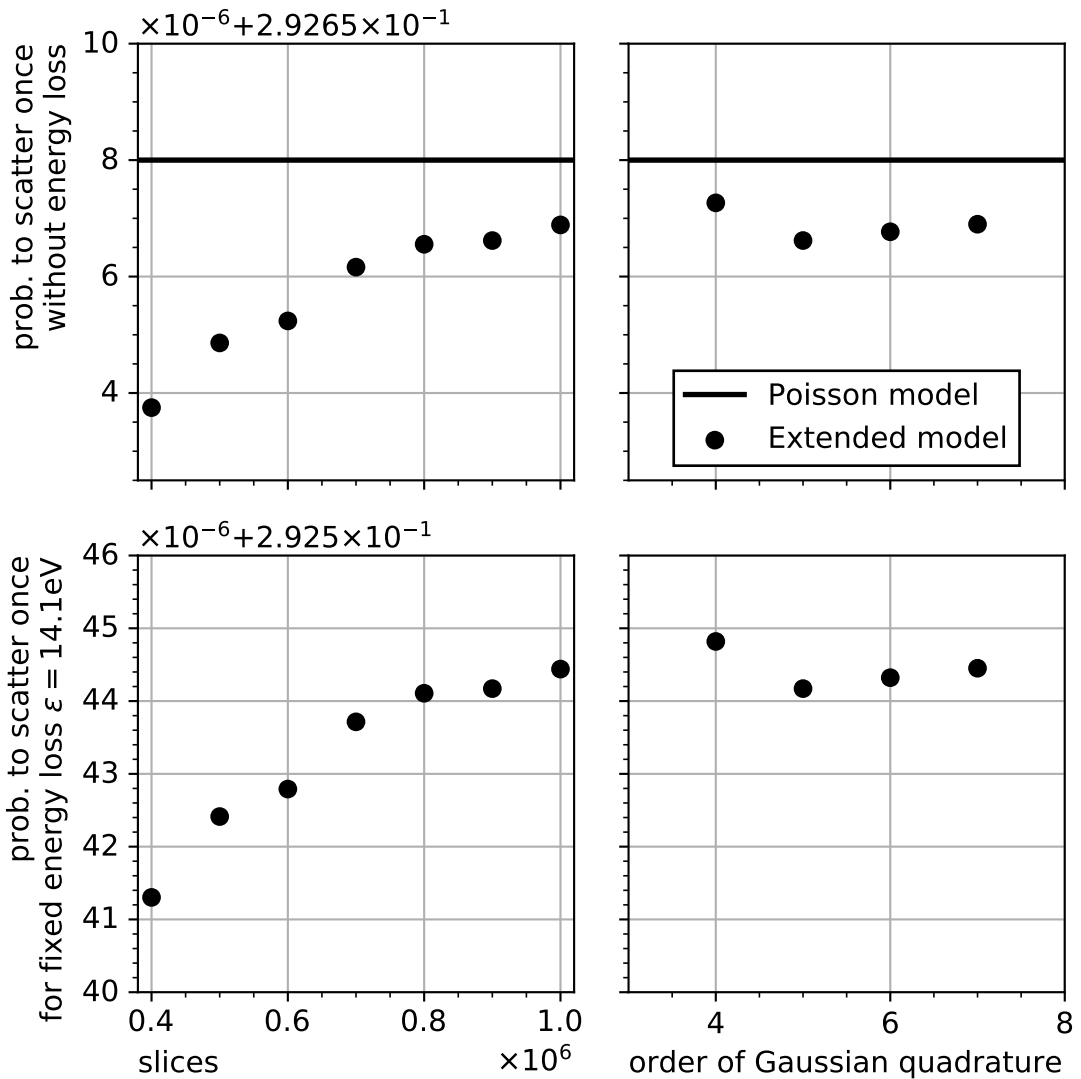


**Figure A.1.: Numerical accuracy of the extended model for the scattering probabilities.** The extended model is given by (A.6). The left column shows the dependence on the number of slices of the WGTS. The right column shows the order of Gaussian quadrature that was used to evaluate the two integrals in the model. For the left column the order of Gaussian quadrature was fixed to 5. For the right column the number of slices was fixed to  $5 \times 10^5$ . The upper row shows the extended model for no energy loss per scattering (markers). Its exact solution is given by the Poisson model (see (4.6)). The lower row shows the model for an energy loss of 14.1 eV per scattering. The results make it plausible to assume a one-sided numerical inaccuracy on the  $10^{-5}$  level for  $N = 10^5$  and using Gaussian quadrature of order 5.

# Acronyms

**BIXS** beta-induced X-ray spectroscopy.

**CKrS** condensed  $^{83m}\text{Kr}$  source.

**CPS** cryogenic pumping section.

**DPS** differential pumping section.

**EMCS** earth magnetic field compensation system.

**FBM** forward beam monitor.

**FPD** focal plane detector.

**FT** First Tritium.

**KNM1** KATRIN Neutrino Mass Measurement 1.

**LARA** laser Raman system.

**LEP** Large Electron Positron Collider.

**LFCS** low-field correction system.

**MAC-E** magnetic adiabatic collimation with electrostatic filtering.

**MLE** maximum likelihood estimator.

**MTD** measurement time distribution.

**PULCINELLA** precision ultra-low current integrating normalization electrometer for low-level analysis.

**RMMS** radial magnetic measuring system.

**SDS** spectrometer and detector section.

**SM** Standard Model of particle physics.

**SSC** source and spectrum calculation.

**STS** source and transport section.

**TLK** Tritium Laboratory Karlsruhe.

**VMMS** vertical magnetic measuring system.

**WGTS** windowless gaseous tritium source.



# Bibliography

- [12] “The positional and angular distribution of molecules flowing through cylindrical tube in free molecular flow”. In: *Physics Procedia* 32 (2012), pp. 513–524. ISSN: 1875-3892. DOI: <https://doi.org/10.1016/j.phpro.2012.03.595>.
- [AA+09] A. Aguilar-Arevalo, C. Anderson, et al. “The miniboone detector”. In: *Nuclear Instruments and Methods in Physics Research Section A: Accelerators, Spectrometers, Detectors and Associated Equipment* 599.1 (2009), pp. 28–46. ISSN: 0168-9002. DOI: [doi.org/10.1016/j.nima.2008.10.028](https://doi.org/10.1016/j.nima.2008.10.028).
- [AA+13] B. Aharmim, S. N. Ahmed, et al. “Combined analysis of all three phases of solar neutrino data from the Sudbury Neutrino Observatory”. In: *Phys. Rev. C* 88 (2 Aug. 2013), p. 025501. DOI: [10.1103/PhysRevC.88.025501](https://doi.org/10.1103/PhysRevC.88.025501).
- [AA+16] Y. Abe, S. Appel, et al. “Measurement of  $\theta_{13}$  in Double Chooz using neutron captures on hydrogen with novel background rejection techniques”. In: *Journal of High Energy Physics* 2016, 163 (Jan. 2016), p. 163. DOI: [10.1007/JHEP01\(2016\)163](https://doi.org/10.1007/JHEP01(2016)163).
- [AB+00] V. Aseev, A. Belesev, et al. “Energy loss of 18 keV electrons in gaseous T and quench condensed D films”. In: *The European Physical Journal D - Atomic, Molecular, Optical and Plasma Physics* 10.1 (Mar. 2000), pp. 39–52. ISSN: 1434-6079. DOI: [10.1007/s100530050525](https://doi.org/10.1007/s100530050525).
- [AB+05] M. Altmann, M. Balata, et al. “Complete results for five years of GNO solar neutrino observations”. In: *Physics Letters B* 616.3 (2005), pp. 174–190. DOI: [doi.org/10.1016/j.physletb.2005.04.068](https://doi.org/10.1016/j.physletb.2005.04.068).
- [AB+15] J. Amsbaugh, J. Barrett, et al. “Focal-plane detector system for the KATRIN experiment”. In: *Nuclear Instruments and Methods in Physics Research Section A: Accelerators, Spectrometers, Detectors and Associated Equipment* 778 (2015), pp. 40–60. ISSN: 0168-9002. DOI: <https://doi.org/10.1016/j.nima.2014.12.116>.
- [AB+16] M. Arenz, M. Babutzka, et al. “Commissioning of the vacuum system of the KATRIN main spectrometer”. In: *Journal of Instrumentation* 11.04 (Apr. 2016), P04011–P04011. DOI: [10.1088/1748-0221/11/04/p04011](https://doi.org/10.1088/1748-0221/11/04/p04011).
- [AB+18] M. Arenz, W.-J. Baek, et al. “The KATRIN superconducting magnets: overview and first performance results”. In: *Journal of Instrumentation* 13.08 (Aug. 2018), T08005–T08005. DOI: [10.1088/1748-0221/13/08/t08005](https://doi.org/10.1088/1748-0221/13/08/t08005).
- [AB+96] K. Assamagan, C. Brönnimann, et al. “Upper limit of the muon-neutrino mass and charged-pion mass from momentum analysis of a surface muon beam”. In: *Phys. Rev. D* 53 (11 June 1996), pp. 6065–6077. DOI: [10.1103/PhysRevD.53.6065](https://doi.org/10.1103/PhysRevD.53.6065).

- [AB17] D. N. Abdurashitov and A. I. o. Belesev. “Electron scattering on hydrogen and deuterium molecules at 14–25 keV by the ‘Troitsk nu-mass’ experiment”. In: *Physics of Particles and Nuclei Letters* 14.6 (Nov. 2017), pp. 892–899. ISSN: 1531-8567. DOI: 10.1134/S1547477117060024.
- [Acc+98] M. Acciarri et al. “Determination of the number of light neutrino species from single photon production at LEP”. In: *Physics Letters B* 431.1 (1998), pp. 199–208. DOI: 10.1016/0370-2693(89)90704-1.
- [AG+09] J. N. Abdurashitov, V. N. Gavrin, et al. “Measurement of the solar neutrino capture rate with gallium metal. III. Results for the 2002–2007 data-taking period”. In: *Phys. Rev. C* 80 (1 July 2009), p. 015807. DOI: 10.1103/PhysRevC.80.015807.
- [Agh+18] N. Aghanim et al. *Planck 2018 results. VI. Cosmological parameters*. 2018. arXiv: 1807.06209 [astro-ph.CO].
- [Ago+18] M. Agostini et al. “Improved limit on neutrinoless double- $\beta$  decay of  $^{76}\text{Ge}$  from GERDA phase II”. In: *Phys. Rev. Lett.* 120.13 (2018), p. 132503. DOI: 10.1103/PhysRevLett.120.132503. arXiv: 1803.11100 [nucl-ex].
- [Ang+05] J. Angrik et al. “KATRIN design report 2004”. In: *Wissenschaftliche Berichte/Forschungszentrum Karlsruhe* 7090 (2005).
- [Ase+11] V. N. Aseev et al. “An upper limit on electron antineutrino mass from Troitsk experiment”. In: *Phys. Rev.* D84 (2011), p. 112003. DOI: 10.1103/PhysRevD.84.112003. arXiv: 1108.5034 [hep-ex].
- [Bab14] M. Babutzka. “Design and development for the rearsection of the KATRIN experiment”. PhD thesis. KIT, 2014. DOI: 10.5445/IR/1000045598.
- [Bar+98] R. Barate et al. “An Upper limit on the tau-neutrino mass from three-prong and five-prong tau decays”. In: *Eur. Phys. J. C2* (1998), pp. 395–406. DOI: 10.1007/s100520050149.
- [Bau14] S. Bauer. “Energy calibration and stability monitoring of the KATRIN experiment”. PhD thesis. WWU, 2014.
- [BC38] H. A. Bethe and C. L. Critchfield. “The formation of deuterons by proton combination”. In: *Phys. Rev.* 54 (4 Aug. 1938), pp. 248–254. DOI: 10.1103/PhysRev.54.248.
- [Bec00] H. Becquerel. “Contribution à l’étude du rayonnement du radium”. In: *J. Phys. Theor. Appl.* 9.1 (1900), pp. 190–199.
- [Bec95] H. Becquerel. “Sur les radiations invisibles émises par les corps phosphorescents”. In: *Comptes rendus Acad des Sciences* 122 (1895), pp. 501–503.
- [Bet39] H. A. Bethe. “Energy production in stars”. In: *Phys. Rev.* 55 (5 Mar. 1939), pp. 434–456. DOI: 10.1103/PhysRev.55.434.
- [Boh32] N. Bohr. “Faraday lecture. Chemistry and the quantum theory of atomic constitution”. In: *J. Chem. Soc.* (0 1932), pp. 349–384. DOI: 10.1039/JR9320000349.
- [BPB01] J. N. Bahcall, M. H. Pinsonneault, and S. Basu. “Solar models: current epoch and time dependences, neutrinos, and helioseismological properties”. In: *Astrophys. J.* 555.2 (July 2001), pp. 990–1012. DOI: 10.1086/321493.
- [BPR15] L. I. Bodine, D. S. Parno, and R. G. H. Robertson. “Assessment of molecular effects on neutrino mass measurements from tritium  $\beta$  decay”. In: *Phys. Rev. C* 91 (3 Mar. 2015), p. 035505. DOI: 10.1103/PhysRevC.91.035505.

- [CD+98] B. T. Cleveland, J. Davis, et al. “Measurement of the solar electron neutrino flux with the Homestake chlorine detector”. In: *Astrophys. J.* 496 (1998), pp. 505–526. DOI: [10.1086/305343](https://doi.org/10.1086/305343).
- [Cha14] J. Chadwick. “Intensitätsverteilung im magnetischen Spectrum der  $\beta$ -Strahlen von Radium B + C”. In: *Verhandl. Dtsc. Phys. Ges.* 16 (1914), p. 383.
- [CR+56] C. L. Cowan, F. Reines, et al. “Detection of the free neutrino: a confirmation”. In: *Science* 124.3212 (1956), pp. 103–104. ISSN: 0036-8075. DOI: [10.1126/science.124.3212.103](https://doi.org/10.1126/science.124.3212.103).
- [DG+62] G. Danby, J. M. Gaillard, et al. “Observation of high-energy neutrino reactions and the existence of two kinds of neutrinos”. In: *Phys. Rev. Lett.* 9 (1962), pp. 36–44. DOI: [10.1103/PhysRevLett.9.36](https://doi.org/10.1103/PhysRevLett.9.36).
- [DT+04] A. Doroshkevich, D. L. Tucker, et al. “Large scale structure in the SDSS galaxy survey”. In: *Astron. Astrophys.* 418 (2004), pp. 7–23.
- [Dyb19] S. Dyba. “Background reduction by the inner wire electrode and set-up of the condensed krypton source at the neutrino mass experiment katrin”. PhD thesis. WWU, 2019.
- [EB+14] M. Erhard, S. Bauer, et al. “High-voltage monitoring with a solenoid retarding spectrometer at the KATRIN experiment”. In: *Journal of Instrumentation* 9.06 (June 2014), P06022–P06022. DOI: [10.1088/1748-0221/9/06/p06022](https://doi.org/10.1088/1748-0221/9/06/p06022).
- [EB+18] M. Erhard, J. Behrens, et al. “Technical design and commissioning of the KATRIN large-volume air coil system”. In: *Journal of Instrumentation* 13.02 (Feb. 2018), P02003–P02003. DOI: [10.1088/1748-0221/13/02/p02003](https://doi.org/10.1088/1748-0221/13/02/p02003).
- [EG+19] I. Esteban, Gonzalez-Garcia, M. C., et al. “Global analysis of three-flavour neutrino oscillations: synergies and tensions in the determination of  $\theta_{23}$ ,  $\delta_{\text{CP}}$ , and the mass ordering”. In: *Journal of High Energy Physics* 2019.1 (Jan. 2019), p. 106. ISSN: 1029-8479. DOI: [10.1007/JHEP01\(2019\)106](https://doi.org/10.1007/JHEP01(2019)106).
- [EH+17] E. Ellinger, N. Haußmann, et al. “Monitoring the KATRIN source properties within the beamline”. In: *Journal of Physics: Conference Series* 888 (Sept. 2017), p. 012229. DOI: [10.1088/1742-6596/888/1/012229](https://doi.org/10.1088/1742-6596/888/1/012229).
- [EW27] C. D. Ellis and W. A. Wooster. “The average energy of disintegration of radium E”. In: *Proc. R. Soc. Lond., A* 117 (1927), p. 109. DOI: [10.1098/rspa.1927.0168](https://doi.org/10.1098/rspa.1927.0168).
- [Fer34] E. Fermi. “Versuch einer Theorie der  $\beta$ -Strahlen”. In: *Zeitschrift für Physik* 88.3 (1934), pp. 161–177. DOI: [10.1007/BF01351864](https://doi.org/10.1007/BF01351864).
- [Fuk+98] Y. Fukuda et al. “Evidence for oscillation of atmospheric neutrinos”. In: *Phys. Rev. Lett.* 81 (1998), pp. 1562–1567. DOI: [10.1103/PhysRevLett.81.1562](https://doi.org/10.1103/PhysRevLett.81.1562).
- [GB+08] S. Grohmann, J. Bonn, et al. “Cryogenic design of the KATRIN source cryostat”. In: *AIP Conference Proceedings* 985.1 (2008), pp. 1277–1284. DOI: [10.1063/1.2908483](https://doi.org/10.1063/1.2908483).
- [Ger75] D. E. Gerhart. “Comprehensive optical and collision data for radiation action. I. H<sub>2</sub>”. In: *The Journal of Chemical Physics* 62.3 (1975), pp. 821–832. DOI: [10.1063/1.430533](https://doi.org/10.1063/1.430533).
- [GG+16] A. Gando, Y. Gando, et al. “Search for Majorana neutrinos near the inverted mass hierarchy region with KamLAND-Zen”. In: *Phys. Rev. Lett.* 117 (8 Aug. 2016), p. 082503. DOI: [10.1103/PhysRevLett.117.082503](https://doi.org/10.1103/PhysRevLett.117.082503).
- [GG+58] M. Goldhaber, L. Grodzins, et al. “Helicity of neutrinos”. In: *Phys. Rev.* 109 (3 Feb. 1958), pp. 1015–1017. DOI: [10.1103/PhysRev.109.1015](https://doi.org/10.1103/PhysRev.109.1015).

- [Gla61] S. L. Glashow. “Partial Symmetries of Weak Interactions”. In: *Nucl. Phys.* 22 (1961), pp. 579–588. DOI: [10.1016/0029-5582\(61\)90469-2](https://doi.org/10.1016/0029-5582(61)90469-2).
- [Gro15] S. Groh. “Modeling of the response function and measurement of transmission properties of the KATRIN experiment”. PhD thesis. KIT, 2015. DOI: [10.5445/IR/1000046546](https://doi.org/10.5445/IR/1000046546).
- [Har15] F. T. Harms. “Characterization and minimization of background processes in the KATRIN main spectrometer”. 51.03.01; LK 01. PhD thesis. KIT, 2015. DOI: [10.5445/IR/1000050027](https://doi.org/10.5445/IR/1000050027).
- [Hig64] P. W. Higgs. “Broken symmetries and the masses of gauge bosons”. In: *Phys. Rev. Lett.* 13 (1964), pp. 508–509. DOI: [10.1103/PhysRevLett.13.508](https://doi.org/10.1103/PhysRevLett.13.508).
- [Jan15] A. Jansen. “The cryogenic pumping section of the KATRIN experiment - design studies and experiments for the commissioning”. PhD thesis. KIT, 2015. DOI: [10.5445/IR/1000047146](https://doi.org/10.5445/IR/1000047146).
- [Kar+19] C. Karl et al. *FITRIUM*. <https://nuserv.uni-muenster.de:8443/karlch/Fitrium>. 2019.
- [KAT19] KATRIN collaboration. *KATRIN analysis and simulations package (KASPER)*. <https://nuserv.uni-muenster.de:8443/katrin-git/kasper>. 2019.
- [KB+05] C. Kraus, B. Bornschein, et al. “Final results from phase II of the Mainz neutrino mass search in tritium decay”. In: *European Physical Journal C* 40 (Apr. 2005), pp. 447–468.
- [KB+19] M. Kleesiek, J. Behrens, et al. “ $\beta$ -decay spectrum, response function and statistical model for neutrino mass measurements with the KATRIN experiment”. In: *The European Physical Journal C* 79.3 (Mar. 2019), p. 204. ISSN: 1434-6052. DOI: [10.1140/epjc/s10052-019-6686-7](https://doi.org/10.1140/epjc/s10052-019-6686-7).
- [KH+18] L. Kuckert, F. Heizmann, et al. “Modelling of gas dynamical properties of the KATRIN tritium source and implications for the neutrino mass measurement”. In: *Vacuum* 158 (2018), pp. 195–205. ISSN: 0042-207X. DOI: <https://doi.org/10.1016/j.vacuum.2018.09.036>.
- [Kir98] T. Kirsten. “GALLEX solar neutrino results”. In: *Progress in Particle and Nuclear Physics* 40 (1998). Neutrinos in Astro, Particle and Nuclear Physics, pp. 85–99. ISSN: 0146-6410. DOI: [doi.org/10.1016/S0146-6410\(98\)00013-1](https://doi.org/10.1016/S0146-6410(98)00013-1).
- [Kle14] M. Kleesiek. “A data-analysis and sensitivity-optimization framework for the KATRIN experiment”. PhD thesis. KIT, 2014. DOI: [10.5445/IR/1000043301](https://doi.org/10.5445/IR/1000043301).
- [Kle19] M. Klein. “Tritium ions in KATRIN: blocking, removal and detection”. PhD thesis. KIT, 2019. 340 pp. DOI: [10.5445/IR/1000093526](https://doi.org/10.5445/IR/1000093526).
- [Kod+01] K. Kodama et al. “Observation of tau neutrino interactions”. In: *Phys. Lett.* B504 (2001), pp. 218–224. DOI: [10.1016/S0370-2693\(01\)00307-0](https://doi.org/10.1016/S0370-2693(01)00307-0).
- [Kos12] A. Kosmider. “Tritium retention techniques in the KATRIN transport section and commissioning of its DPS2-F cryostat”. PhD thesis. KIT, 2012. DOI: [10.5445/IR/1000028959](https://doi.org/10.5445/IR/1000028959).
- [Kuc16] L. Kuckert. “The windowless gaseous tritium source of the katrin experiment - characterisation of gas dynamical and plasma properties”. PhD thesis. KIT, 2016. 296 pp. DOI: [10.5445/IR/1000065077](https://doi.org/10.5445/IR/1000065077).

- [LH+18] J. Letnev, W. Hazenbiller, et al. “Technical design and commissioning of a sensor net for fine-meshed measuring of the magnetic field at the KATRIN spectrometer”. In: *Journal of Instrumentation* 13.08 (Aug. 2018), T08010–T08010. DOI: 10.1088/1748-0221/13/08/t08010.
- [Liu73] J. W. Liu. “Total inelastic cross section for collisions of H<sub>2</sub> with fast charged particles”. In: *Phys. Rev. A* 7 (1 Jan. 1973), pp. 103–109. DOI: 10.1103/PhysRevA.7.103.
- [Liu87] J. W. Liu. “Total cross sections for high-energy electron scattering by H<sub>2</sub> (<sup>1</sup> Σ<sub>g</sub><sup>+</sup>), N<sub>2</sub> (<sup>1</sup> Σ<sub>g</sub><sup>+</sup>), and O<sub>2</sub> (<sup>3</sup> Σ<sub>g</sub><sup>-</sup>)”. In: *Phys. Rev. A* 35 (2 Jan. 1987), pp. 591–597. DOI: 10.1103/PhysRevA.35.591.
- [LL02] T. J. Loredo and D. Q. Lamb. “Bayesian analysis of neutrinos observed from supernova SN 1987A”. In: *Phys. Rev. D* 65 (6 Feb. 2002), p. 063002. DOI: 10.1103/PhysRevD.65.063002.
- [LY56] T. D. Lee and C. N. Yang. “Question of parity conservation in weak interactions”. In: *Phys. Rev.* 104 (1 1956), pp. 254–258. DOI: 10.1103/PhysRev.104.254.
- [MNS62] Z. Maki, M. Nakagawa, and S. Shoichi. “Remarks on the unified model of elementary particles”. In: *Progress of Theoretical Physics* 28.5 (Nov. 1962), pp. 870–880. DOI: 10.1143/PTP.28.870.
- [MS86] S. P. Mikheev and A. Y. Smirnov. “Resonant amplification of neutrino oscillations in matter and solar neutrino spectroscopy”. In: *Nuovo Cim.* C9 (1986), pp. 17–26. DOI: 10.1007/BF02508049.
- [Noe18] E. Noether. “Invarianten beliebiger Differentialausdrücke”. In: *Nachrichten von der Gesellschaft der Wissenschaften zu Göttingen, Mathematisch-Physikalische Klasse* 1918 (1918), pp. 37–44.
- [OW08] E. W. Otten and C. Weinheimer. “Neutrino mass limit from tritium beta decay”. In: *Rept. Prog. Phys.* 71 (2008), p. 086201. DOI: 10.1088/0034-4885/71/8/086201. arXiv: 0909.2104 [hep-ex].
- [Pon58] B. Pontecorvo. “Inverse beta processes and nonconservation of lepton charge”. In: *Sov. Phys. JETP* 7 (1958), pp. 172–173.
- [PR+12] M. Prall, P. Renschler, et al. “The KATRIN pre-spectrometer at reduced filter energy”. In: *New Journal of Physics* 14.7 (July 2012), p. 073054. DOI: 10.1088/1367-2630/14/7/073054.
- [PSB15] F. Priester, M. Sturm, and B. Bornschein. “Commissioning and detailed results of KATRIN inner loop tritium processing system at Tritium Laboratory Karlsruhe”. In: *Vacuum* 116 (2015), pp. 42–47. ISSN: 0042-207X. DOI: <https://doi.org/10.1016/j.vacuum.2015.02.030>.
- [PW+08] W. Pauli, V. Weisskopff, et al. *Wissenschaftlicher Briefwechsel mit Bohr, Einstein, Heisenberg u.a. Band II: 1930–1939*. Springer Berlin Heidelberg, 2008. ISBN: 9783540788010.
- [Röll15] M. Röllig. “Tritium analytics by beta induced X-ray spectrometry”. PhD thesis. 2015. 202 pp. DOI: 10.5445/IR/1000054050.
- [Rut99] E. Rutherford. “VIII. Uranium radiation and the electrical conduction produced by it”. In: *The London, Edinburgh, and Dublin Philosophical Magazine and Journal of Science* 47.284 (1899), pp. 109–163. DOI: 10.1080/14786449908621245.
- [Sal68] A. Salam. “Weak and electromagnetic interactions”. In: *Conf. Proc.* C680519 (1968), pp. 367–377.

- 
- [Sch13] M. R. H. Schlösser. “Accurate calibration of the raman system for the karlsruhe tritium neutrino experiment”. PhD thesis. 2013. DOI: [10.5445/IR/1000034967](https://doi.org/10.5445/IR/1000034967).
- [Sei19] H. Seitz-Moskaliuk. “Characterisation of the KATRIN tritium source and evaluation of systematic effects”. PhD thesis. KIT, 2019.
- [Tan+18] M. Tanabashi et al. “Review of particle physics”. In: *Phys. Rev. D* 98 (3 Aug. 2018), p. 030001. DOI: [10.1103/PhysRevD.98.030001](https://doi.org/10.1103/PhysRevD.98.030001).
- [Tho97] J. J. Thomson. “XL. Cathode rays”. In: *The London, Edinburgh, and Dublin Philosophical Magazine and Journal of Science* 44.269 (1897), pp. 293–316. DOI: [10.1080/14786449708621070](https://doi.org/10.1080/14786449708621070).
- [TM+09] T. Thümmler, R. Marx, et al. “Precision high voltage divider for the KATRIN experiment”. In: *New Journal of Physics* 11.10 (Oct. 2009), p. 103007. DOI: [10.1088/1367-2630/11/10/103007](https://doi.org/10.1088/1367-2630/11/10/103007).
- [Tro19] N. R.-M. Trost. “Modeling and measurement of Rydberg-state mediated background at the KATRIN main spectrometer”. 51.03.01; LK 01. PhD thesis. KIT, 2019. 178 pp. DOI: [10.5445/IR/1000090450](https://doi.org/10.5445/IR/1000090450).
- [UR+09] M. Ubieto-Díaz, D. Rodríguez, et al. “A broad-band FT-ICR penning trap system for KATRIN”. In: *International Journal of Mass Spectrometry* 288.1 (2009), pp. 1–5. ISSN: 1387-3806. DOI: <https://doi.org/10.1016/j.ijms.2009.07.003>.
- [Val09] K. Valerius. “Spectrometer-related background processes and their suppression in the KATRIN experiment”. PhD thesis. WWU, 2009.
- [WA+57] C. S. Wu, E. Ambler, et al. “Experimental test of parity conservation in beta decay”. In: *Phys. Rev.* 105 (4 Feb. 1957), pp. 1413–1415. DOI: [10.1103/PhysRev.105.1413](https://doi.org/10.1103/PhysRev.105.1413).
- [Wei38] C. F. Weizäcker. “Über Elementumwandlungen im Innern der Sterne”. In: *Phys. Zeit.* 39 (633 1938), p. 46.
- [Wei67] S. Weinberg. “A model of leptons”. In: *Phys. Rev. Lett.* 19 (21 Nov. 1967), pp. 1264–1266. DOI: [10.1103/PhysRevLett.19.1264](https://doi.org/10.1103/PhysRevLett.19.1264).
- [Wol78] L. Wolfenstein. “Neutrino oscillations in matter”. In: *Phys. Rev. D* 17 (1978). [,294(1977)], pp. 2369–2374. DOI: [10.1103/PhysRevD.17.2369](https://doi.org/10.1103/PhysRevD.17.2369).
- [YP+17] C. Yèche, Palanque-Delabrouille, Nathalie, et al. “Constraints on neutrino masses from Lyman-alpha forest power spectrum with BOSS and XQ-100”. In: *JCAP* 1706.06 (2017), p. 047. DOI: [10.1088/1475-7516/2017/06/047](https://doi.org/10.1088/1475-7516/2017/06/047). arXiv: [1702.03314 \[astro-ph.CO\]](https://arxiv.org/abs/1702.03314).
- [Zee03] A. Zee. *Quantum Field Theory in a Nutshell*. Princeton University Press, 2003. ISBN: 9780691010199.
- [Zub11] K. Zuber. *Neutrino Physics, Second Edition*. Series in High Energy Physics, Cosmology and Gravitation. Taylor & Francis, 2011. ISBN: 9781420064711.